Geothermics 64 (2016) 344–361

Contents lists available at ScienceDirect

Geothermics

journal homepage: www.elsevier.com/locate/geothermics

Coastal thermal springs in a foreland setting: The Santa Cesarea Terme system (Italy)

F. Santaloia[a,*], L.E. Zuffianò[a], G. Palladino[b], P.P. Limoni[a], D. Liotta[c,d], A. Minissale[e], A. Brogi[c], M. Polemio[a]

[a] Research Institute for Geo-Hydrological Protection, National Research Council of Italy (CNR), Via Amendola 122/I, 70126 Bari, Italy
[b] Geology and Petroleum Geology, University of Aberdeen, Aberdeen, UK
[c] Department of Earth and Geoenvironmental Sciences, University of Bari, Via Orabona 4, 70125 Bari, Italy
[d] Institute of Geosciences and Earth Resources, National Research Council of Italy (CNR), Via G. Moruzzi 1, 56124 Pisa, Italy
[e] Institute of Geosciences and Earth Resources, National Research Council of Italy (CNR), Via La Pira 4, 50121 Florence, Italy

ARTICLE INFO

Article history:
Received 12 November 2015
Received in revised form 8 April 2016
Accepted 22 June 2016
Available online 10 July 2016

Keywords:
Foreland
Thermal springs
Carbonate reservoir
Apulia

ABSTRACT

Carbonate aquifers in foreland tectonic settings can host important thermal springs although located in areas commonly not characterized by regional high heat flow values. In these cases, when thermal springs are located close or along the coastlines the subaerial and/or submarine thermal springs constitute the outflow of marine groundwater, flowing through localized fractures and karsitic rock-volumes. This is the case of springs occurring along the south-easternmost portion of the Apulia region (Southern Italy) where few sulphurous and warm waters (22–33 °C) outflow in partially submerged caves located along the shoreline, thus supplying the historical spas of Santa Cesarea Terme. Here, with the aim to define the origin of the thermal fluids and their deep path, we carried out the geo-structural survey of the area and detailed hydrogeological and geochemical analyses of the thermal spring fluids. In particular, the isotopes $\delta^{18}O$, δD, ^{13}C in DIC, $^{34}S_{sulphate}$, $^{34}S_{sulphide}$, $^{3}He/^{4}He$ ratio and ^{13}C in CO_2 were used to define the origin of the thermal water and the recharge mechanism of the geothermal system while the isotopes ^{3}H and ^{14}C were determined for estimating the age of the thermal waters, resulting in older than roughly twenty thousands years BP. The results indicate that the thermal springs are fed by marine water, having reached Santa Cesarea Terme through a localized fracture network. This affects the evaporitic and carbonatic rocks that characterize the substratum of the Adriatic Sea in the offshore.

1. Introduction

Most of the high temperature (>150 °C) water resources (Muffler and Cataldi, 1978) are mostly associated with recent volcanic activity occurring near plate boundaries, in the surroundings of crustal and mantle hot spot anomalies, or in continental extensional tectonic environments where coeval magma intrusions are volumetrically significant, thus determining heat flow values (>100 mW/m^2; Goldstein et al., 2011).

Thermal springs are some of the recognisable surface manifestations of thermal fluid circulation at depth. This can naturally occur in a volcanic context (e.g., hot springs on the island of Java in Purnomo and Pichler, 2014 and references therein) and/or in areas where cooling magma is present only at mid-crustal depth (i.e. Larderello, Brogi et al., 2005). Obviously, thermal springs can be influenced by primary permeability differences among geological bodies, but very often, their location is driven by fault systems, defining permeable rock-volumes in rocks where the original texture would not permit a water storing. (i.e. Bürchau springs in Rolker et al., 2015; Valdieri thermal springs in Baietto et al., 2008; southern Canadian Cordillera springs in Grasby and Hutcheon, 2001; Florida springs in Fanning et al., 1981).

As it concerns the Italian peninsula, thermal springs are connected to the original variability of permeability of the geological bodies and tectonic structures (e.g. Minissale, 2004). However this is a matter of fact that such a springs are mostly concentrated in the inner part of Apennines (Tyrrhenian sector; Fig. 1) where heat flow is high (>100 mW/m^2) and it is characterized by reduced lithospheric and crustal thickness (about 50 and 25 km thick, respectively; Nicolich, 2001). Conversely, there are very few

* Corresponding author.
E-mail address: f.santaloia@ba.irpi.cnr.it (F. Santaloia).

http://dx.doi.org/10.1016/j.geothermics.2016.06.013
0375-6505/

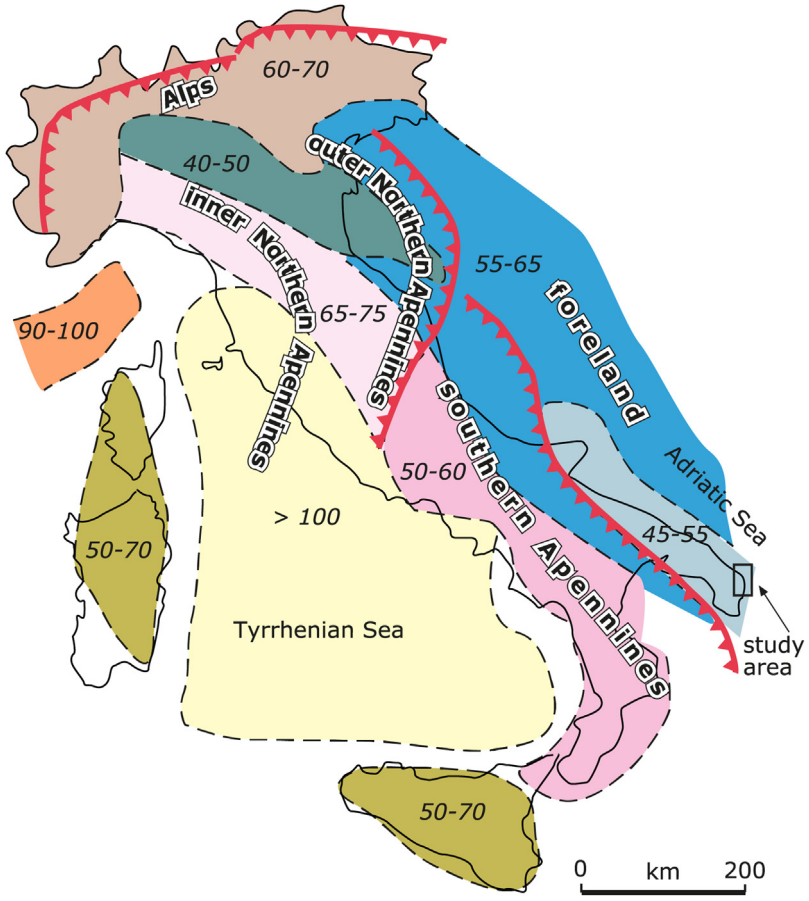

Fig. 1. Heat flow map of Italy: values of the conductive heat flow are given in mW/m^2 (after Della Vedova et al., 2001; redrawn).

thermal springs are few in the eastern side of Italy, where heat flow decreases to 30–40 mW/m^2 (Adriatic sector; Della Vedova et al., 2001) and lithosperic and crustal thickness is about 120 and 45 km, respectively (Nicolich, 2001). These differences account for different tectonic environments that are extensional to the west, and compressional to the east, respectively (Mostardini and Merlini, 1986; Patacca and Scandone, 2007). Nevertheless, foreland areas, although characterized by low heat flow, are also affected by geothermal manifestations in spot-areas, with low temperature (about 25–28 °C) geothermal fluids at ground surface. This is the case of Santa Cesarea Terme thermal springs, located in the Apulia carbonate platform (Fig. 1), interpreted as the foreland (Ricchetti et al., 1988) of the southern Apennines collisional belt (Cretaceous-Pleistocene).

This paper focuses on the geothermal system associated with the Santa Cesarea springs, flowing out along a narrow coastal sector of the Salento peninsula (Figs. 1 and 2a) part of the Apulia carbonate platform, representing the southern Apennines foreland. As well known, seawater intrusion occurs along this coastal sector (Maggiore and Pagliarulo, 2004; Romanazzi et al., 2015). The Santa Cesarea spring water, with temperature ranging from 24 °C to 30 °C, is rich in sulphur (Calò and Tinelli, 1995) and nowadays is employed in a spa.

Several hypotheses on the origin of this warm groundwater were already proposed from volcanic (Milani, 1815) to a connate origin, associated to nearby hydrocarbon resources, flowing through fault zones dislocating the Dinaric foredeep (Maggiore and Pagliarulo, 2004). On the other hand, the sulphur content in the spring water might result from the sulphurization of deep groundwater, due to the activity of sulphate-reducing bacteria (Biginelli, 1899) affecting either the organic matter at depth or the coal included within Miocene outcrops (Zezza, 1980).

In order to contribute to the understanding of the Santa Cesarea Terme low-temperature geothermal system (referred as SCT system hereafter), we conducted a multidisciplinary research integrating the results from structural geology, hydrogeology, and hydrogeochemistry fields. In particular, the structural analyses were aimed at defining the structural channels, which controlled the circulation of the SCT thermal waters, whereas the groundwater flow and recharge were studied by hydrogeological in-situ investigations. Finally, the origin of the geothermal fluids and the role of water–rock interaction processes were argued from the hydrogeochemical analyses.

2. Geological and hydrogeological setting

The SCT system is hosted by the southern Apulian foreland (Ricchetti et al., 1988; Fig. 1). This is made up, from the bottom to the top, of: (a) pre-Cambrian crystalline basement postulated from geophysical data (Finetti, 2005 and references herein); (b) a Permian-Triassic succession, represented by siliclastic and evaporitic (anhydrite and dolostone) sediments respectively, thicker than 3 km as encountered in an oil well located around 250 km to the North-West of Santa Cesarea Terme village (Puglia 1 well; ViDEPI Project, 2009), in particular the evaporite level is 400 m thick at least as indicated in the boreholes (Ricchetti et al., 1988) (c) Jurassic-Cretaceous carbonate succession, whose thickness surely overpasses 4.5 km (Ricchetti et al., 1988; Ugento 1 well in Fig. 2; ViDEPI Project, 2009); (d) Oligocene to Pleistocene carbonate to clastic sediments, extensively outcropping inland.

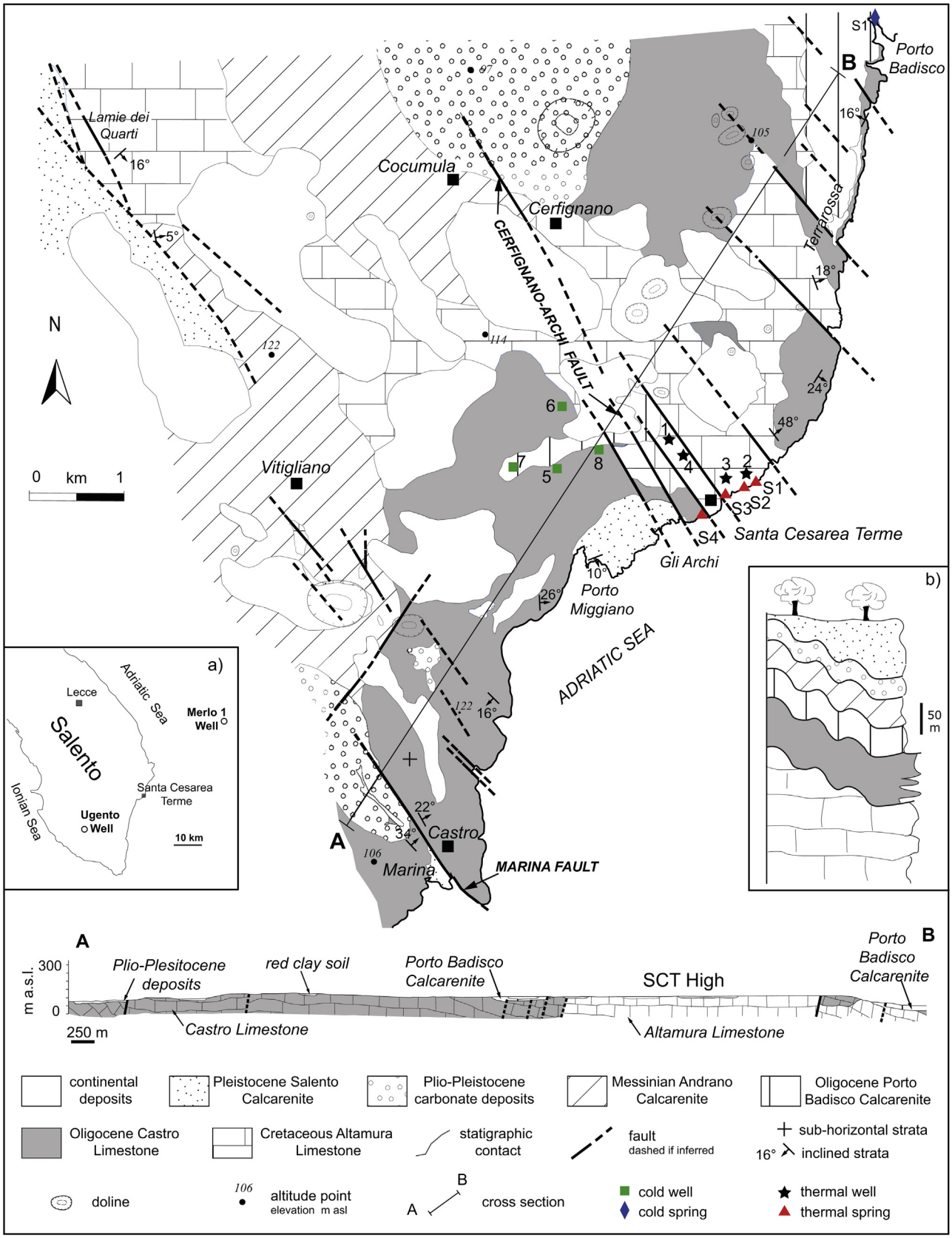

Fig. 2. Geological map of the study area with a representative geological section; (a) sketch of the Salento Peninsula with the location of the oil wells mentioned in the text; (b) stratigraphic log.

With reference to the studied area, the structural deeper outcropping geological body is the 600 m thick Altamura Limestone Formation (Late Cretaceous; Ricchetti et al., 1988), made up of well-bedded limestone, dolomitic limestone and dolostone (Fig. 2). This is overlain unconformably by the Late Oligocene Castro coral reef limestone Formation (Pomar et al., 2014 and references herein), as shown in Fig. 2. Both these formations are unconformably covered (Fig. 2) by poorly bedded neritic calciclastic deposits, known as the Oligocene Porto Badisco Calcarenite and the Messinian Andrano Calcarenite Formations (Bosellini et al., 1999; Pomar et al., 2014). Finally, cyclical Plio-Pleistocene shallow-water carbonate deposits rest at the top of the previously described successions (Fig. 2). Among these, the Pleistocene Salento Calcarenite Formation (Bossio et al., 2005 and references herein) deposited in a tectonically active slope environment, as testified by slumps and synsedimentary structures (Fig. 3).

All carbonate formations show intense karstification, both at the surface and at depth. Here caves and karsified and fissured horizons are interbedded with more compact limestone strata (Pepe and Parise, 2013; Romanazzi et al., 2015). The Mesozoic-Oligocene carbonate succession is part of the wide unconfined aquifer (defined as limestone aquifer herein), recharged through rainfall infiltration (Romanazzi et al., 2015), which involves more than the whole Salento (Fig. 1).

At SCT, the aquifer groundwater (calcium-bicarbonate water in Cotecchia, 1977; Polemio et al., 2009), hereinafter called fresh groundwater, floats on intruding seawater. However, a transition zone exists between the pure fresh groundwater and the saline water due seawater intrusion: within the transition zone the water salinity rapidly increases to depth from less than 0.5 g/l as total of dissolved solids (as TDS hereafter) to about 40 g/l of TDS, representing the seawater salinity (Cotecchia, 1977; Cotecchia et al., 2005; Polemio et al., 2009). Below the bottom of this zone spatially variable as main function of potentiometric head of fresh groundwater but roughly located at 150 m below sea level, salinity does not change with depth (Cotecchia, 1977; Cotecchia et al., 2005).

Groundwater temperature of limestone aquifer, usually equal to 14.5–16 °C inland, slightly increases along the flow paths, up to about 19–20 °C close to the coast (Cotecchia, 1977; Cotecchia et al., 2005; Romanazzi et al., 2015).

All summarised peculiarities of fresh groundwater were confirmed for the SCT sector.

The structure of the SCT offshore substratum is known through interpretation of reflection seismic lines (Mocnik, 2008; Del Ben et al., 2015 and reference herein) and stratigraphic borehole log (Merlo 1 well, ViDEPI Project, 2009). The Mesozoic-Tertiary carbonate platform is affected by normal faults defining a pelagic domain with isolated platforms (South Apulian basin; Mocnik, 2008; Del Ben et al., 2015) where Messinian deposits (evaporite, clays with organic matter and mudstone, about 30 m thick in Merlo 1 well at a structural high), and 500 m thick Plio-Quaternary marine clastic sediments. As in other Mediterranean basins, these Messinian deposits are thicker toward the basin depocentre (Roveri et al., 2014).

The tectonic activity of the geological structures defining the Apulian offshore is documented by historical (during 1743 in Favali et al., 1990) and recent earthquakes as it was in 1974 (M = 4.9) and in 2008 (M = 2.9); the epicentres were located 60–120 km offshore (INGV, 2006; Mocnik, 2008). All of them were solved by focal mechanism, considering a strike-slip component (INGV, 2006; Mocnik, 2008; Di Bucci et al., 2011 and references herein).

3. Methods and data collection

The geothermal exploration concerned about 50 km^2 (Fig. 2) an area including SCT and where fieldwork geological survey, hydrogeological field-testing and geochemical analyses were conducted.

The fieldwork was based on the classical approach of field mapping and structural geology, collecting structural and kinematic data in stations distributed in the study area on the basis of location of the main structures and suitable outcrops.

With regards to the hydrogeological analysis, sixteen stations for temperature measurements were selected. Considering thermal waters as those with temperature above 20 °C, therefore we selected 4 thermal and 2 cold springs, 4 thermal and 5 cold wells, seawater (Fig. 2).

Groundwater potentiometric head was measured within inland wells under no-pumping conditions (static head). From December 2011 to January 2012, groundwater temperature at Fetida and Gattulla springs (#S1, #S3 in Fig. 2) was measured hourly by means of probes connected to data loggers. The flow rate of these springs was acquired using an acoustic Doppler current profiler in their outflow section in the underground caves. Besides, electrical conductivity and water temperature were monitored at depth in both thermal wells n. 1 and n. 4 (Fig. 2) while the redox potential was measured in well n.1 only.

Groundwater samples for geochemical and isotopic analyses were collected both at spring sources and at wells (Tables 1–3). The water sampling was performed by standard sampling procedures, a part from well 3 where static sampling was used (two samples, at 45 m and 52 m below the ground surface; see also in Tables 1–2). Moreover, seven samples were taken at different depth during the drilling of well 4, after its flushing. All water samples were collected and stored in high-density polyethylene bottles (250 mL) with watertight caps. Samples for cation analysis were preserved by using an acidifying container (concentrated HNO_3 to a pH ≤ 2) while water samples for metals determination were firstly filtered

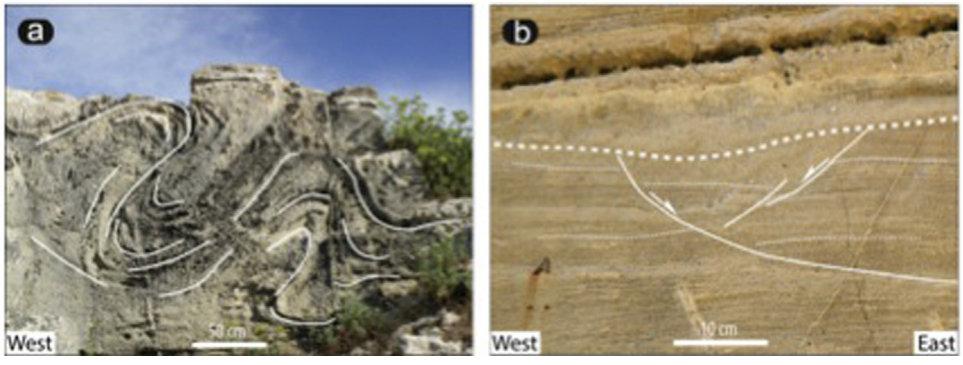

Fig. 3. Syn-sedimentary structures affecting the Quaternary calcarenite: (a) Highly non-cylindrical folds (slump) dissected by fractures; (b) Syn-sedimentary normal faults with centimetre to decimeter vertical offsets.

Table 1
Chemical and isotopic composition of water samples. Z) Altitude, WD) bottom well depth, EC) electric conductivity at 25 °C. n d = not determined.

	Sample	Type-Name	Z (m a.s.l.)	WD (m)	T (°C)	E. C. (mS/cm)	pH (–)	Eh (mV)	δD (‰ SMOV)	$\delta^{18}O$ (‰ SMOV)	^{3}H (U.T.)	$\delta^{13}C$ PDB	^{14}C (BP)	^{14}C (pcm)	$^{34}S/S_{tot}$ (V-CDT)
Spring	S1	Thermal–Fetida	–		27.0	53.4	7.10	−337	0.60	0.05	1.03	−4.59	n d	n d	19.7
	S2	Thermal–Sulfurea	–		21.1	59.3	7.69	−85	−13.8	−2.74	1.40	−1.41	n d	n d	19.4
	S3	Thermal–Gattulla	–		24.5	41.4	6.20	−265	−0.40	0.37	1.56	−8.35	n d	n d	19.6
	S4	Thermal–Solfatara	–		25.7	40.1	7.54	−220	−6.70	−1.47	n d	n d	n d	n d	n d
	S5	Cold–Porto Badisco	–		21.0	7.60	7.80	169	n d	n d	n d	n d	n d	n d	n d
	S6	Cold–Acquaviva	–		17.8	27.2	7.53	210	n d	n d	n d	n d	n d	n d	n d
Wells	1	Thermal	115.4	205.0	27.5	62.1	6.88	−263	5.9	1.78	0.46	−1.55	19849	8.45	20.0
	2	Thermal	33.57	50.0	32.7	64.2	6.71	−268	5.9	1.57	0.33	−1.95	21050	7.54	19.9
	3–45 m	Thermal	41.76	200.0	21.4	7.09	7.57	−237	n d	n d	n d	n d	n d	n d	n d
	3–52 m				–	–	–	–	−21.7	−3.39	n d	n d	n d	n d	n d
	4–125 m	Thermal (Vigor)	115.0	300.0	22.0	4.21	6.99	−136	n d	n d	n d	n d	n d	n d	n d
	4–151 m				24.0	52.5	7.80	−399	n d	n d	n d	n d	n d	n d	n d
	4–300 m				27.0	52.2	7.99	−296	n d	n d	n d	n d	n d	n d	n d
	5	Cold	121.0	–	19.2	0.44	8.70	−21	−34.2	−5.47	4.60	−12.81	n d	n d	n d
	6	Cold	117.0	–	19.3	3.88	8.21	80	−30.3	−5.39	n d	n d	4268	58.5	n d
	7	Cold	123.0	130.0	20.1	2.29	8.27	−39	−30.2	−5.57	n d	−12.83	n d	n d	n d
	8	Cold	112.0	–	19.8	0.95	8.08	74	−33.3	−5.64	n d	−13.48	n d	n d	n d
	9	Cold	108.6	116.4	16.0	0.87	7.05	75	−33.2	−5.78	2.80	−10.58	n d	n d	n d
Sea	10	Sea Water	–	–	19.1	60.3	8.20	169	7.1	1.48	n d	n d	n d	n d	n d

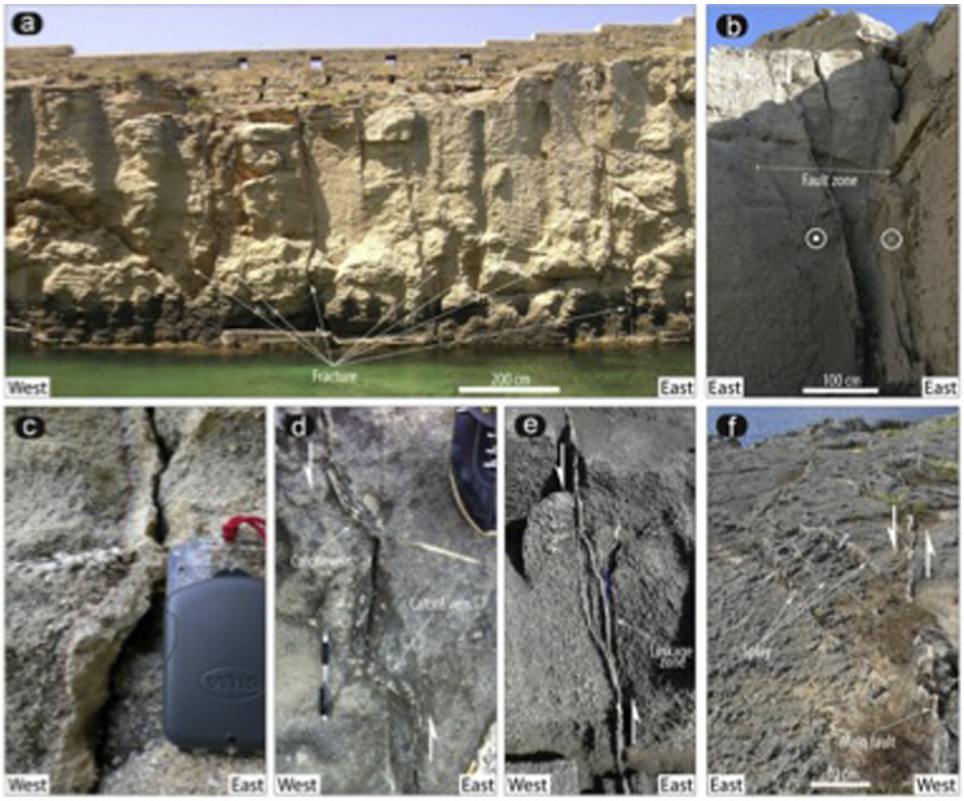

Fig. 4. Examples of brittle structures affecting the Quaternary calcarenite; (a) m-thick spaced, sub-vertical, fractures cemented by calcite; (b) particular of a left-lateral oblique-slip fault zone characterized by anastomosed shear fractures cemented by calcite; (c) detail of the shear fracture cemented by calcite, supporting for infiltration of fluids; (d) extensional jogs filled by calcite in a left-lateral strike-slip fault zone; (e) anastomosed left-lateral strike-slip shear fractures cemented by calcite; (f) Splay system developed within the damage zone of a main left-lateral strike-slip fault.

through a cellulose acetate membrane (pore size 0.2 micrometres) and secondly, these were acidified by nitric acid.

Samples electrical conductivity (EC), pH, temperature (T), redox potential (Eh) and dissolved oxygen (O_2) were measured directly in the field by means of a multiparametric probe. Chemical and isotopic compositions were produced at the CNR-IGG laboratories, following standard procedures by: (a) ion-chromatography for cations and anions (Table 2); (b) volumetric titration for HCO_3^- (Table 2); (c) inductively coupled plasma mass spectrometry for trace elements (Table 3) and isotopes (Table 1).

Isotope ^{34}S (thermal water sampled at wells #2 and #4), ^{3}H and ^{18}O, were ascertained by the mass spectrometer at the Environmental Isotope Laboratory – Earth & Environmental Sciences Department (University of Waterloo, Canada). Finally, the isotope enrichment factor, ε equal to $\delta^{34}S_{sulphate} - \delta^{34}S_{sulphur}$, was defined following Wynn et al. (2010).

One stripped gas was obtained by the #2 thermal well by syringing 500 ml of water under vacuum, of which composition was obtained after gas-chromatographic analysis.

In the following, $^{18}O/^{16}O$ and D/H ratio are expressed with the typical δ notation referred to as V-SMOW, while the abundant ratio of ^{34}S and ^{32}S is generally given as $\delta^{34}S$ relatively to VCDT. The overall precision of the analyses on major ions, is within 5%. Differently, the experimental errors are estimated in ± 0.1‰ for $\delta^{13}C$, ± 1.0‰ for $\delta^{2}H$, ± 0.3‰ for ^{34}S (dissolved in both SO_4^{2-} and H_2S) and ± 0.5‰ for ^{18}O dissolved in SO_4^{2-}.

^{3}H and ^{14}C activities of the dissolved inorganic carbon in the water were used to constrain the age estimates of the study waters. The concentration of ^{3}H was estimated by means of inductively coupled plasma mass spectrometry (Table 1). Conversely, the concentration of ^{14}C for radiocarbon groundwater dating was achieved by an accelerator mass spectrometry at the Diagnostic and Dating Centre of the Salento University (Italy). The results are shown in Table 1, expressed as both uncorrected BP apparent ages and percent modern carbon (pcm).

4. Data analyses

4.1. Structural data

The relationships between brittle geological structures and geothermal fluid flow were investigated through a structural and kinematic survey of the study area. The most significant structural and kinematic data are from the Salento Calcarenite succession, the most recent sediment cropping out.

The deformation is characterized by subvertical, N-S trending faults (Fig. 4a), and associated minor fractures (Fig. 4b). The damage zone (Fig. 4b) is decimeter in thickness whereas the slip zone displays a cemented cataclasite (Fig. 4c). Fluids circulated through the catacaclasite and extensional jogs providing calcite veins (Fig. 4d). No clear kinematic indicators on the fault surfaces have been recognized but the angular relationships between the main faults and associated fractures clearly suggest a left lateral strike-to-oblique slip movement (Fig. 4d,e and f). This kinematics is also confirmed by the detailed structural survey carried out in a key-area, as illustrated in Fig. 5, where the left lateral component is dominant.

Deformation in the calcareous substratum is defined by normal to left-lateral oblique slip faults. The most significant structure crops out in the Castro Harbor (Fig. 6) where one of this fault clearly dissects the carbonate succession and the overlying Quaternary deposits (Fig. 6a,c and d). The damage zone, about 8 m thick, is

Table 2
Chemical composition (in mg/L) of water samples. n d = not determined. n p = not present.

Sample	Li^+	Na^+	K^+	NH_4^+	Mg^{2+}	Ca^{2+}	Sr^{2+}	F^-	I^-	Cl^-	HCO_3^-	Br^-	NO_3^-	SO_4^{2-}	S^{2-}
S1	0.42	9219	347	1.41	959	908	12.7	118	0.29	17304	228.8	82.6	41.5	2878	3.12
S2	0.05	12130	383	0.00	1358	784	10.4	9.14	n d	20212	202.8	83.7	50.7	3322	0.61
S3	0.27	5415	224	0.79	5766	574	7.59	76.4	0.28	9035	309.9	39.7	30.6	1833	2.51
S4	0.34	10258	264	49.1	768	672	15.9	18.8	n d	16429	244.0	76.3	0.00	1926	n d
S5	0.03	1351	72.8	0.95	164	165	1.47	10.9	4.40	2189	311.1	7.98	25.6	424	n.p
S6	0.05	2210	152	0.00	514	154	0.00	0.38	19.2	4538	299.0	15.2	8.98	802	n.p
1	0.55	13477	509	0.00	1385	1311	18.7	36.1	0.33	23923	195.2	113	29.5	3813	21.7
2	0.45	13484	506	1.63	1339	1553	20.9	54.8	0.31	24369	187.0	123	62.9	3848	31.6
3–45 m	0.02	628	38.2	0.00	55.6	75.4	0.00	0.54	1.46	1109	354.0	5.83	0.9	128	n.p
3–52 m	0.14	4630	245	0.00	685	485	0.01	0.60	0.27	9220	213.0	25.6	0.55	1167	7.50
4–125 m	0.02	643	25.5	0.00	72.0	118	0.25	0.37	n d	1260	311.0	4.00	22.0	156	n p
4–151 m	0.25	12269	378	0.00	1005	492	13.0	1.60	n d	22681	189.1	74.0	11.9	2640	0.33
4–300 m	0.45	10180	438	0.00	991	1218	19.1	1.88	n d	17858	213.5	77.0	0.00	2087	0.74
5	0.00	15.4	0.24	0.24	2.99	64.9	0.36	1.26	n d	26.5	170.9	0.13	12.8	6.60	n.p
6	0.01	544	26.3	4.29	63.2	132	0.00	2.58	0.28	1118	274.6	4.42	47.5	140	n.p
7	0.01	319	11.4	0.00	38.8	102	0.26	2.55	3.53	645	268.5	2.51	7.72	83.0	n.p
8	0.00	60.1	30.6	0.00	13.1	90.5	0.47	0.93	0.63	137	241.0	0.49	74.9	35.2	n.p
9	0.00	66.5	36.9	5.84	32.2	110	0.34	6.38	0.57	138	392.8	0.32	23.1	67.5	n.p
10	0.18	11617	417	0.00	1489	520	14.2	10.6	n d	23371	189.1	94.2	0.00	2859	n.p

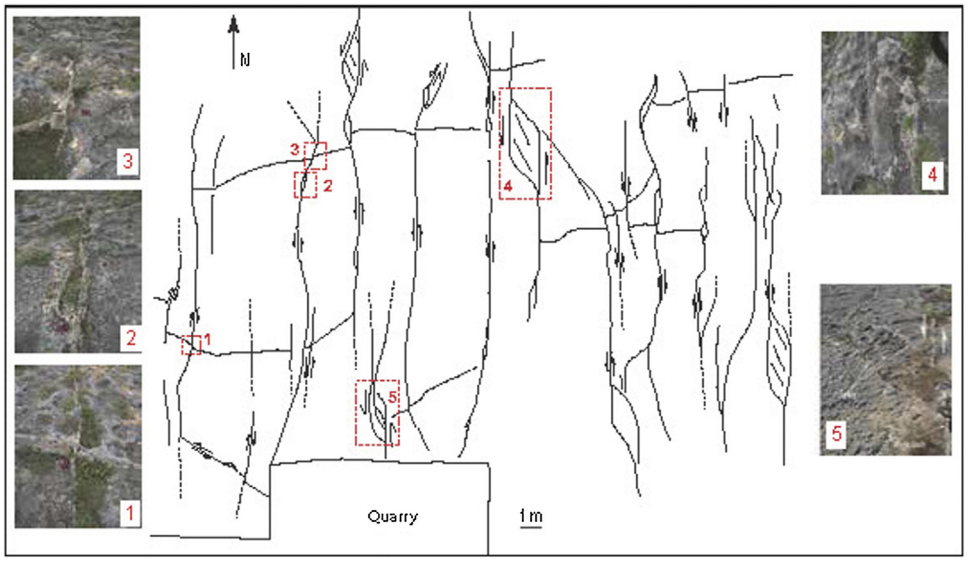

Fig. 5. Scan lines resulted from structural survey performed at Porto Miggiano (locality in Fig. 2).

mostly localized in the fault hanging wall. It is defined by coalescing fractures with attitudes coherent with the fault geometry and kinematics and by a cataclastic breccia (Fig. 6d) made up of carbonate elements in calcareous cement. Kinematic indicators consist of grooves, mega-grooves and slickensides, visible on slip surfaces both on the main fault scarp (Fig. 6b and e) or on minor surfaces within the cataclasite (Fig. 6f).

The Castro Marina fault is therefore an example of the high-angle faults dissecting the carbonate rocks with a NW-SE trend in the surroundings of the study area (Fig. 2). Thus, in their arrangement, this fault system defines structural highs where the villages of Castro and Santa Cesarea are located (Fig. 2), referred as Castro High and SCT High in the following.

As regards the age of activity of this system, the Castro Marina fault, as well as the other companion structures, dissects the Salento Calcarenite succession as recognized in the geological map (Fig. 2). On the basis of this evidence and on the fact that this fault cross-cuts the Quaternary breccia, we interpret such a fault system as active since post-Pleistocene, at least. Therefore, in the period encompassed by Pleistocene and Present, the area is affected by two coeval fault systems, N-S and NW-SE trending, respectively.

Regarding the kinematic and geometric compatibility between the two different fault systems, some considerations could be proposed: (a) the occurrence of extensional jogs and linkage zones NW-SE oriented in the Salento Calcarenite succession (Fig. 4) suggests a possible explanation for a coherent deformational context in which N-S and NW-SE faults can be framed; (b) it is a matter of fact that, at map scale, all the N-S trending faults are not highlighted, although this can be a consequence of the recent fault activity, implying reduced offsets; (c) the NW-SE faults display a left-lateral oblique-slip movement and a significant offset, exceeding 10 m, implying a fault activity older than the N-S oriented fault system. It is therefore suggested that the Pleistocene-Present deformation determined the N-S fault trend and partially reactivated the already existing NW-SE trending faults. In this framework, a localized improvement of permeability, along almost vertical structural channels is envisaged.

Finally, the described fault systems had a strong influence on the development of the main karst landforms (doline, karst valley and

Table 3
Chemical composition (in μg/L) of water samples. –not determined.

Sample	Ag	Al	As	Au	B	Ba	Be	Bi	Cd	Co	Cr	Cs	Cu	Fe	Hg	Ho	Mn	Mo	Ni	Pb	Rb	Sb	Se	Si	U	V	W	Zn
S1	<5	<100	64.0	<5	6057	50.0	<5	<5	<5	<2	<50	1.00	24.0	<1000	<10	<1	<5	<10	<20	1740	111	<5	158	4405	<2	139	<2	<50
S2	<5	<100	258	<5	5208	40.0	<5	<5	5	6	<50	2.00	11.0	<1000	<10	<1	12	<10	<20	5722	116	6.00	206	4353	<2	89.0	<2	500
S3	<5	<100	<50	<5	3327	37.0	<5	<5	<5	<2	<50	1.00	<10	<1000	<10	<1	5	<10	<20	1132	71.0	<5	111	<4000	<2	23.0	<2	<50
S5	<0.5	<10	8.0	<0.5	527	39.1	<0.5	<0.5	<0.5	<0.2	<5	<0.1	2.00	<100	<1	<0.1	<0.5	2	<2	341	13.9	<0.5	20.0	4067	1.6	16.0	<0.2	<5
S6	<0.5	2.87	14.5	<0.5	1.56	28.0	<0.5	<0.5	<0.5	<0.2	<5	0.20	–	4.58	<1	<0.1	0.11	–	<2	–	31.8	0.12	–	–	–	–	<0.2	<5
1	<5	<100	67.0	<5	8906	51.0	<5	<5	<5	<2	<50	2.00	<10	<1000	<10	<1	9.00	<10	<20	3375	159	<5	226	4152	<2	68.0	<2	<50
2	<5	<100	59.0	<5	10590	57.0	<5	<5	<5	<2	<50	2.00	<10	<1000	<10	<1	24.0	<10	572	4137	165	<5	270	4973	<2	<20	<2	<50
3–45 m	<5	4.89	2.14	<5	1.66	24.3	<5	<5	<5	<2	<50	0.15	<10	115	<10	<1	37.6	<10	<20	–	21.7	0.08	–	–	<2	<20	<2	<50
3–52 m	<5	3.70	16.4	<5	3.06	31.0	<5	<5	<5	<2	<50	0.40	<10	88.6	<10	<1	25.0	<10	<20	–	46.4	0.14	–	–	<2	<20	<2	<50
5	<0.05	0.20	0.13	<0.05	0.01	2.45	<0.05	<0.05	–	–	<5	0.10	–	35.4	<1	<0.1	26.1	–	–	–	0.12	0.06	–	–	–	–	<0.2	–
6	<0.05	3.44	1.53	<0.05	0.18	7.47	<0.05	<0.05	–	–	<5	0.10	–	66.1	<1	<0.1	3.03	–	–	–	4.00	0.04	–	–	–	–	<0.2	–
7	<0.05	0.27	0.26	<0.05	0.04	2.39	<0.05	<0.05	–	–	<5	0.10	–	354	<1	<0.1	44.6	–	–	–	0.60	0.03	–	–	–	–	<0.2	–
8	<0.05	6.23	0.80	<0.05	0.04	3.44	<0.05	<0.05	–	–	<5	0.10	–	9.27	<1	<0.1	2.10	–	–	–	14.4	0.05	–	–	–	–	<0.2	–
9	<0.05	6.00	1.00	<0.05	38.0	47.8	<0.05	<0.05	0.11	0.02	7.20	0.01	7.70	47.0	<1	<0.1	5.61	0.60	0.30	26.20	1.20	0.10	1.20	3815	1.92	4.10	<0.2	10.7

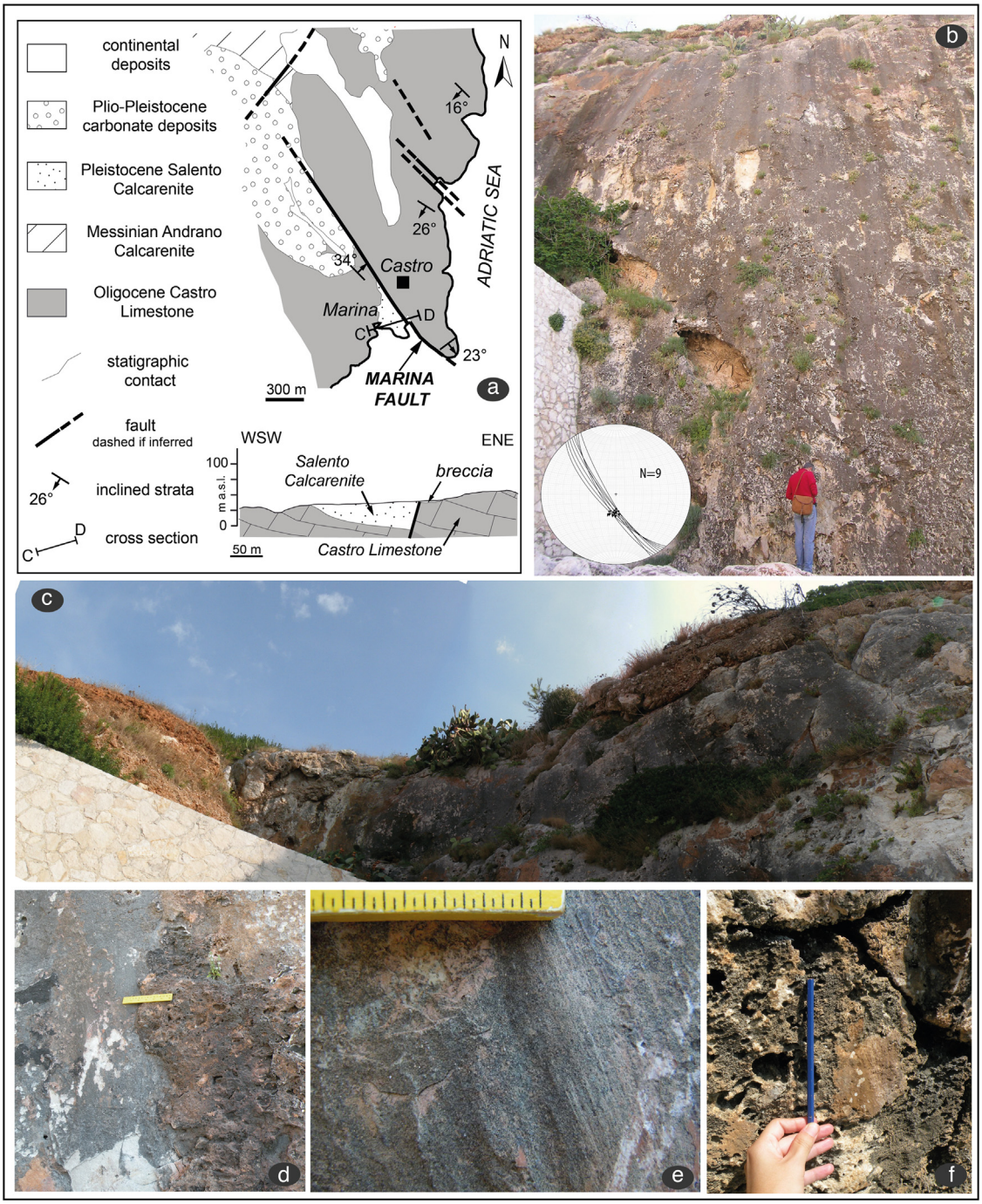

Fig. 6. (a) Geological map of the Castro area with a representative geological section – (b) Main fault scarp exposed in the Castro harbour and relative stereographic diagram (equiareal diagram, lower hemisphere) indicating a main left-lateral oblique-slip kinematics; (c) Quaternary breccias dissected by the Castro Fault attesting a Quaternary age of the Castro Fault; (d) epigean calcite cementing the Castro Fault cataclasite indicating the infiltration of meteoric water within the fault zone; (e–f) kinematic indicators on the slip surface consist of mechanical striation (e) and calcite + Fe-hydroxides thin crusts (f).

so on) identified in the studied territory (Ardizzone et al., 2012). In particular, the cave growing directions (thermal and no thermal caves) resulted also to be deeply influenced by the described fault systems, thus indicating the structural control on the fluid flow.

4.2. Hydrogeological data

Fig. 7a shows the piezometric surface contour map for the limestone aquifer revealing a general groundwater flow direction towards southeast or seaward. This confirms the common trend characterizing the whole Salento region, where fresh and cold groundwater of the limestone aquifer flows from inland recharge areas to the outflow coastal areas (Cotecchia et al., 2005). In this framework, the piezometric head changes from about 2 m a.s.l. to 0 m a.s.l. in SCT (Fig. 7a).

The limestone groundwater temperature changes from 16 °C (outside the study area, in the recharge zone) to about 20 °C (Fig. 7b); the electric conductivity is less than 3.6 mS/cm (Fig. 7c) while the total dissolved solids are generally less than 500 mg/L; the redox potential ranges close to zero (Fig. 7d).

Taking into consideration that the T, EC, and Eh, the higher absolute values (maps in Fig. 7b–d) were recorded in the wells where

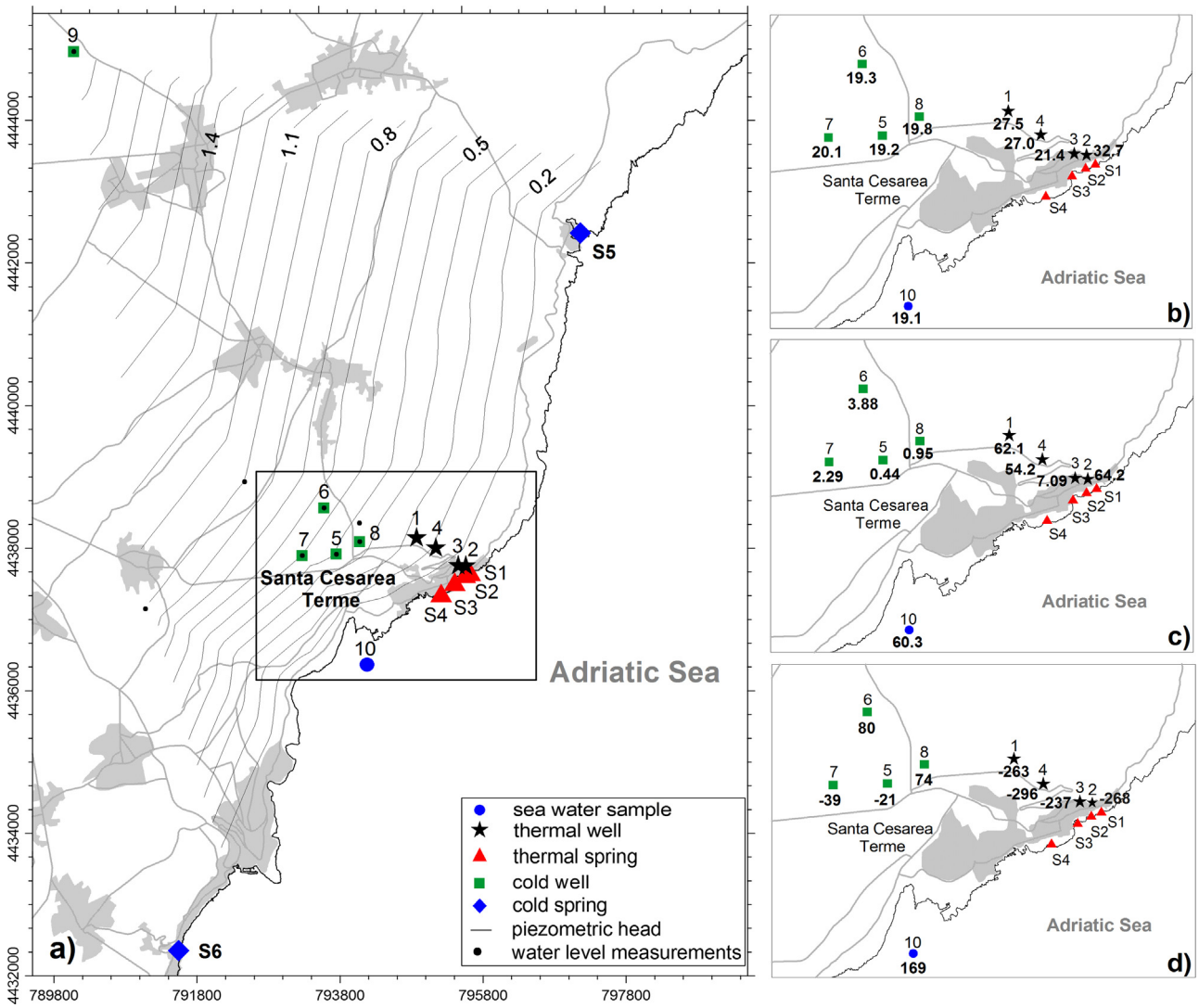

Fig. 7. Piezometric surface map (limestone aquifer, m a.s.l.), well and spring code (Table 1) (a); Monitoring survey carried out in June 2012 and in June 2014 only for well 4: temperature map (°C, b), electrical conductivity map (mS/cm at 25 °C, c), and Eh map (mV, d).

the thermal springs and wells are settled (Figs. 2 and 7). Here, in fact, groundwater temperatures ranges between 22 and 33 °C with a TDS up to 5 mg/L. Their related piezometric head is fairly higher than in the nearby cold wells (e.g. 1 m a.s.l. estimated for thermal well 4 respect to 0.6 m a.s.l. obtained for cold well 7; see Fig. 2).

The water temperature, the water level, and the outflow yield measured in the Fetida and Gattulla springs ensued to change during the time. As shown in Fig. 8a, Fetida spring displays a temperature ranging between 14.6 °C and 28.4 °C while its water level is from −0.726 m to 0.708 m, both of them respect to the sea level. On the other hand, the Gattulla spring is characterized by the water temperature from 13.6 °C to 29.7 °C and water level between −0.421 m s.l. and 0.864 m s.l (Fig. 8b). The flow yield was measured two times resulting 0.283-0.312 m^3/s and 0.0014-0.0097 m^3/s for Fetida and Gattulla springs, respectively. These temporal changes are explained as effects of the tide fluctuations (Visintin, 1944; Calò and Tinelli, 1995) affecting the coastal sector under study.

Fig. 9 shows the multiparametric logs achieved for the thermal wells n. 1 and n.4 (Fig. 2), where water table is s. T and EC, measured for both wells, increase to depth while Eh decreases moving downwards in well 1 (Fig. 9). In this latter, abrupt changes were recorded for all the measured parameters almost at the same depth, of about 138 m b.g.l. (below ground level). However, after that, groundwater values resulted fairly constant: T shifted from 24 °C to 28.1 °C, EC changed from 10 mS/cm to 63 mS/cm, and Eh from almost 20 mV down to −400 mV (Fig. 9a). Contrariwise, EC changed suddenly with depth and T increased gradually from 19.5 °C to 27.4 °C (Fig. 9b) Moreover, EC reached its maximum (67 mS/cm) at about 295 m b.g.l. (Fig. 9b). Only to the temperature log of well 4 (Fig. 9b) shows a local increase, that can be explained as the consequence of hotter water plumes, coming from more fractured and karstified horizons intercepted at that depth.

4.3. Geochemical data

Tables 1–3 report the chemical and the isotopic composition determined for all the water samples. Samples #1 and # 2 represent the thermal waters, sample #5 is indicative of the fresh groundwater and sample # 10 is the seawater; all the other samples have a variable geochemistry, as discussed later on.

The thermal waters could be classified as Na-Cl type while the fresh water as Ca-HCO_3 type (Fig. 10).

The thermal waters have the highest concentrations of Ca^{2+} and the lowest content of Mg^{2+} (Table 1); they are under-

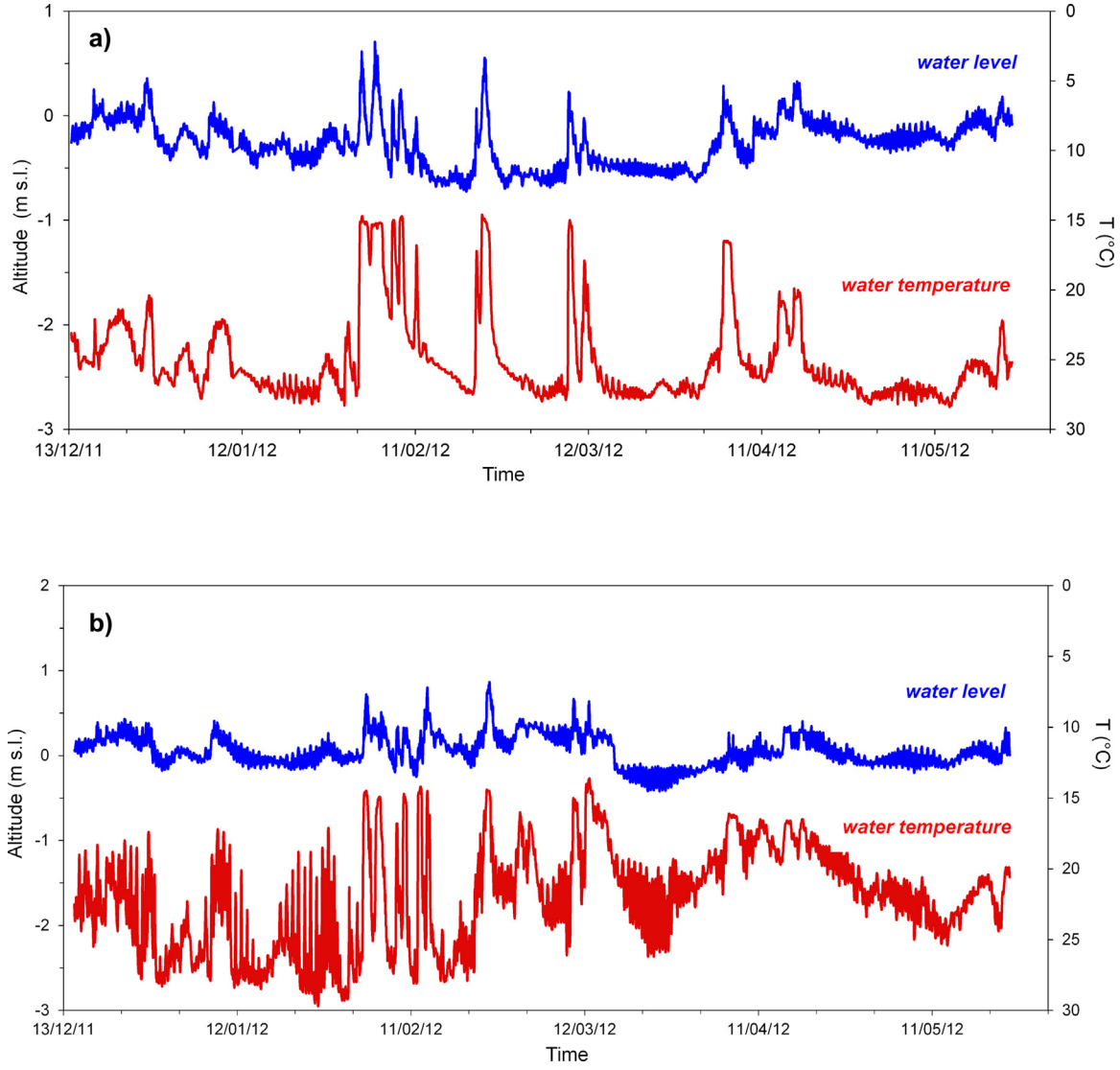

Fig. 8. Variations in water temperature and water level measured in the Fetida (a) and Gattula (b) thermal springs.

saturated in calcite and dolomite ($SI_{calcium}$ = −0.38/−0.50 and $SI_{dolomite}$ = −0.30/−0.63) while they result nearly saturated with respect to gypsum (Fig. 11). The thermal waters have also the highest Li^+, Sr^{2+}, B^{3+} and Br^- contents (Tables 2–3). Taking 4.6 mg/L as reference value for the boron in seawater being almost constant throughout the world seas (White, 1957; Kharaka and Hanor, 2003), the B/Br ratio calculated for the thermal samples (i.e. 78.81 and 86.10 μg/L for #1 and #2, respectively) results higher than the one characterizing seawater (#10: 48.83 μg/L) and freshwater (#5: = 0.08 μg/L). Differently, the Cl/Br ratio for thermal waters is equal to 211.71–198.12 mg/L resulting so lower than seawater value (248.10 mg/L) and comparable to the one from freshwater (203.45 mg/L). The thermal waters display also the highest computed Sr/Ca + Mg and Li/Cl ratios (Fig. 12).

As shown in Tables 1–3 and Figs. 10–12, the chemical content of the other water samples varies from the thermal and sea waters composition (samples from the thermal springs and wells #3 and 4) or from the groundwater and seawater composition (cold springs and samples #6–#9). In particular, the seawater sample and the fresh one represent the end members of the mixing line plotted in the Langelier-Ludwig diagram (Fig. 10a) along which the cold-water samples (#6–#9 in Fig. 10a) are dispersed being them a mixture of fresh groundwater and seawater. The mixing processes among fresh, thermal and seawater taking place at SCT system is peculiarly indicated by the waters sampled at different depths in well 4 (Fig. 10b). Here the shallower one (sample 4–125) indicate a composition of the fresh water fairly mixed with seawater while the deepest sample (sample 4–300) accounts for thermal water, similarly to #1 (Fig. 10b). A higher degree of mixing with seawater is recorded by # 4–151 (Fig. 10b). In summary a geochemical water stratification is indicated as it should be expected.

The composition of the stripped gas obtained by the #2 thermal well indicated a content of about 72% N_2, 25% CO_2 and of about 1% CH_4. These values suggest a relevant atmospheric N_2-rich component and a reduced component of deep CO_2. In fact, this CO_2 having a $\delta^{13}C$ of carbon at −1.95‰ (PDB) clearly derives from the limestone dissolution. The corrected $^3He/^4He$ ratio (Craig et al., 1978) was also measured in doubled. In terms of R/Ra, where R is the ratio in the sample and Ra the ratio in the air, the average value is of about 0.4 suggesting a crustal origin eventually affected by air (R/Ra = 1 in air).

Regarding the isotopic composition of analysed samples, Fig. 13a shows the δD–$\delta^{18}O$ values compared with the Global Meteoric Water Line (GMWL; Craig, 1961) and the Mediterranean Meteoric

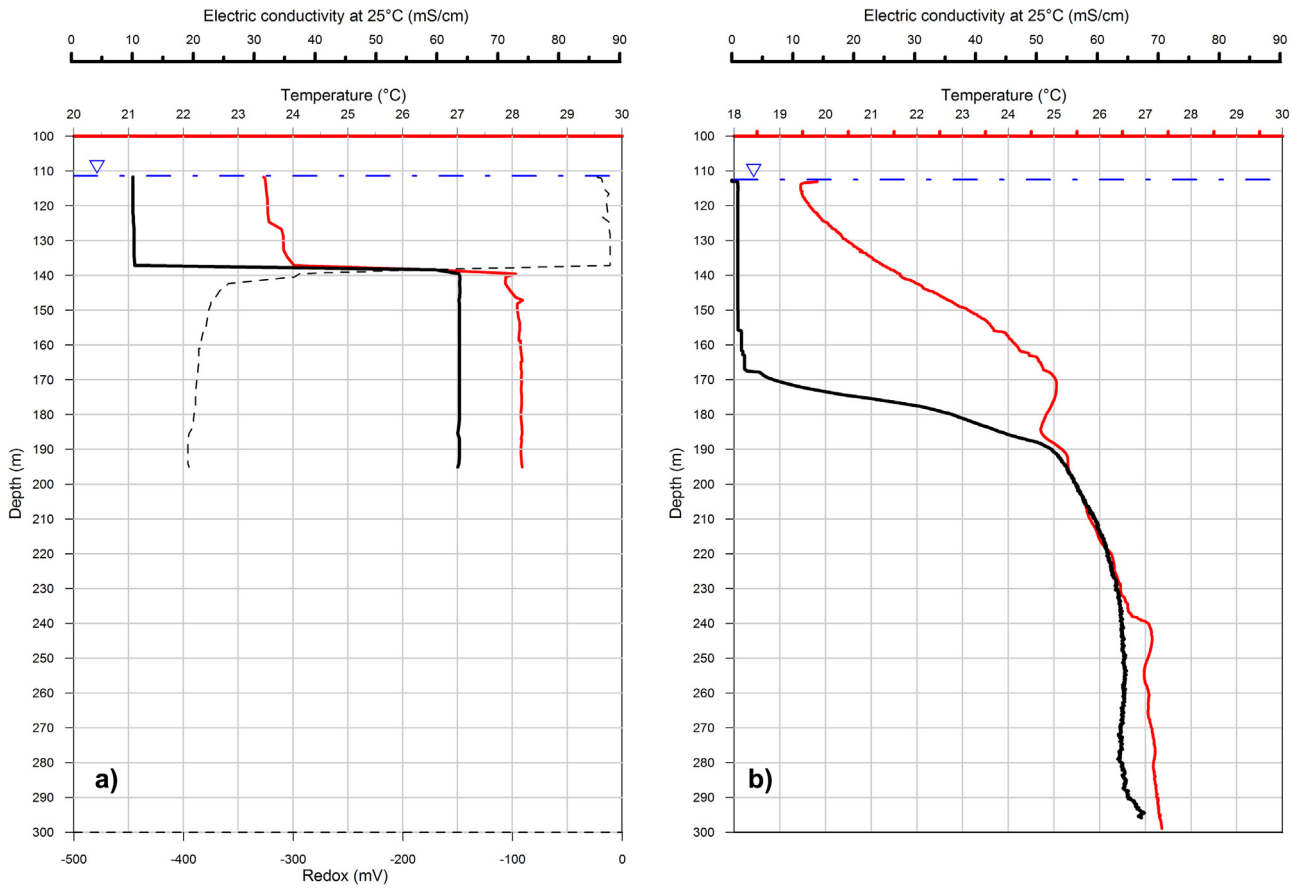

Fig. 9. Multiparametric logs for thermal wells 1 (a) and 4 (b).

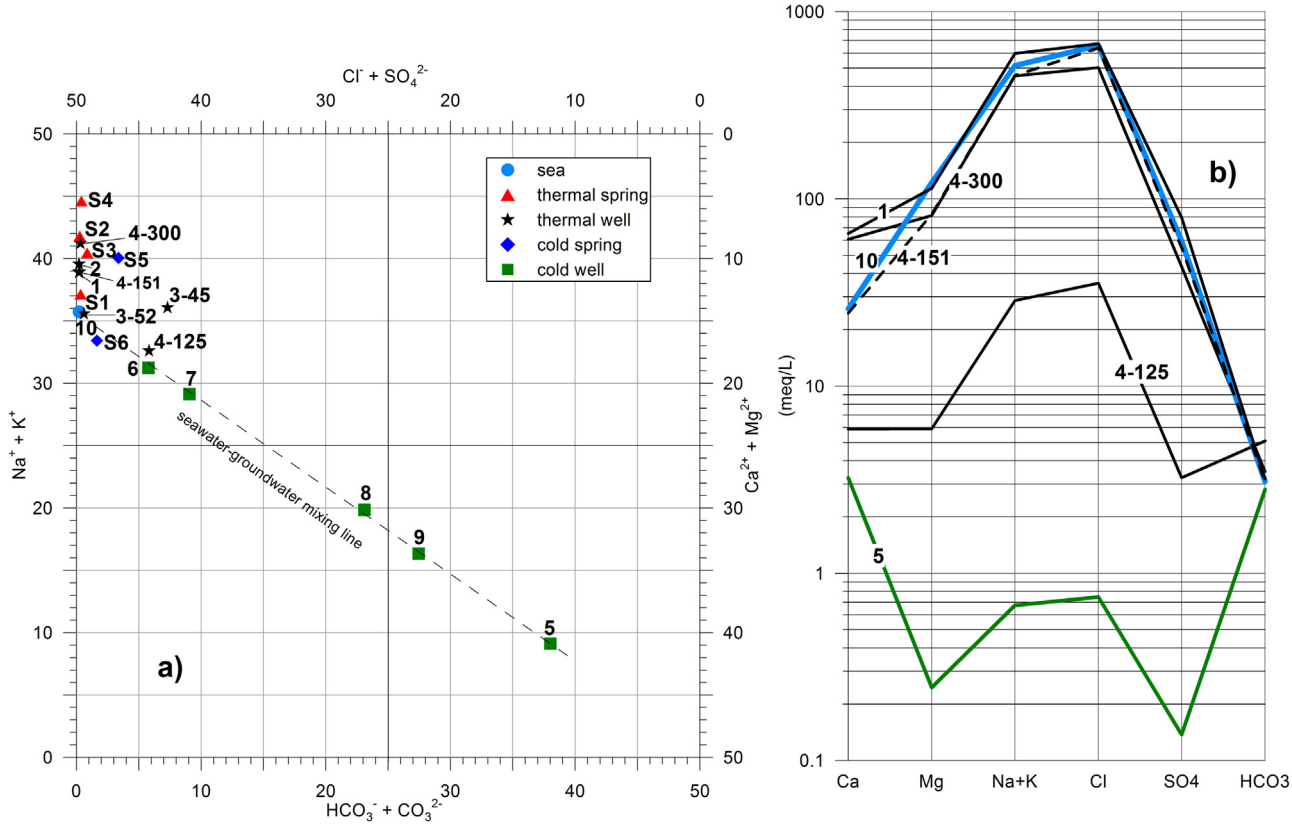

Fig. 10. Langelier-Ludwig (a) and Schoeller (b) diagrams of the sampled waters; data from Zuffianò et al. (2013) and new data.

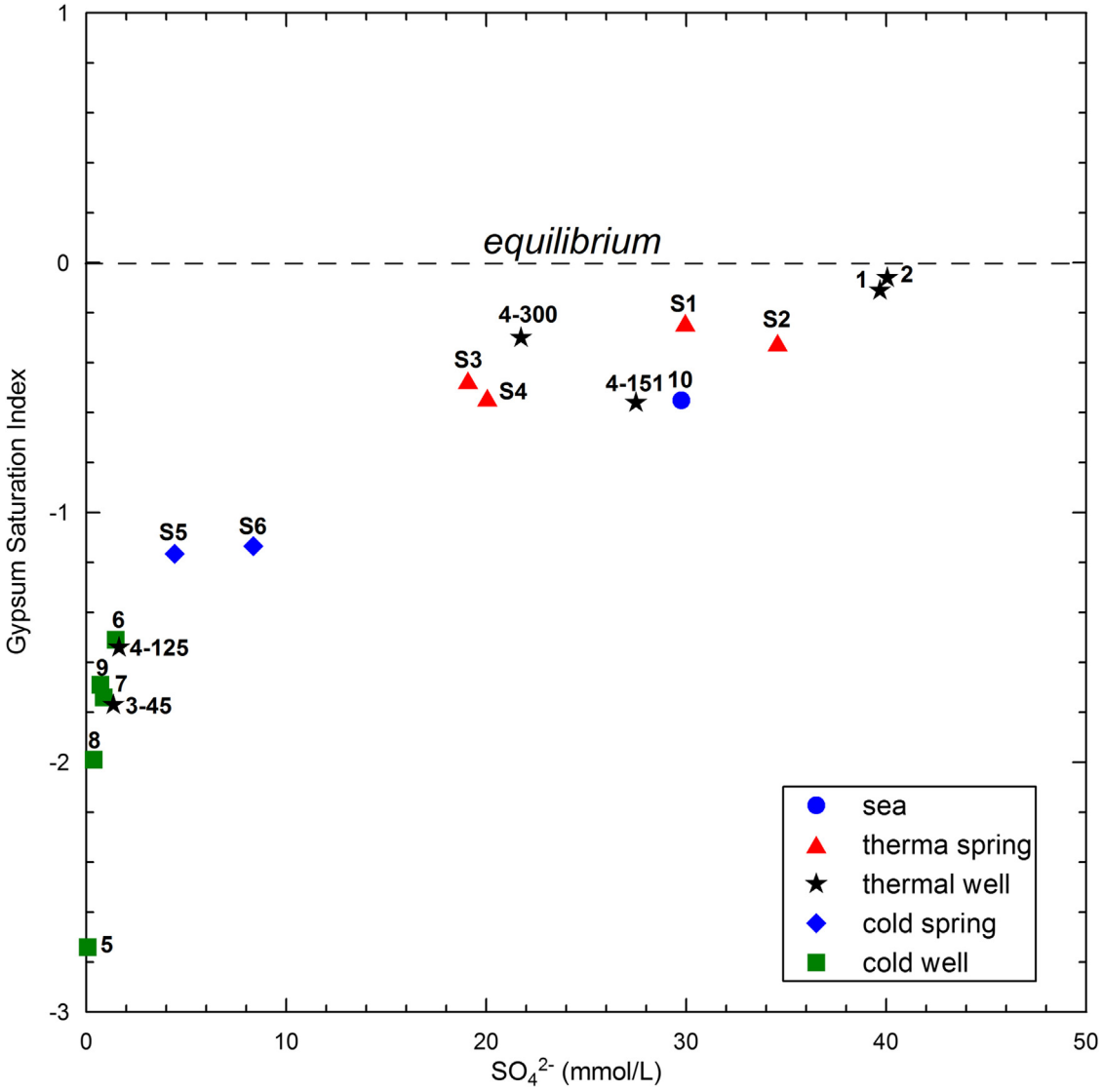

Fig. 11. Correlation between gypsum saturation index and sulphate concentrations in the sampled waters.

Water Line (MMWL; Gatt and Carmi, 1970). The Local Water Line (LWL), obtained interpolating all the analysed data, is also plotted in the same diagram. As a result, the cold water samples (#5–#9) fall between the MMWL and GMWL lines, thus suggesting a meteoric origin, with recharge areas located at altitudes less than 500 m a.s.l. (Minissale and Vaselli, 2011). All the other samples plot to the right of both these water lines (Fig. 13a), especially thermal samples #1 and #2 which record a slightly positive $\delta^{18}O$-shift with respect to seawater (Fig. 13a), probably connected to an evaporation process as here explained later on. The thermal spring waters (#S1, #S2, #S3, #S4) exhibit δD and $\delta^{18}O$ values along a line between the meteoric samples (#5 to #9) and the saline ones, suggesting therefore the occurrence of a mixing of fresh, thermal and marine waters.

The thermal waters #1 and #2 have very low tritium content (0.46 and 0.33 ±0.3 TU), which is less than the present seawater content (2.2 TU; Sivan et al., 2005). Differently higher tritium contents, up to almost 5 TU, are recorded in the cold-water samples (Fig. 13b). These results suggest a very long residence time (>50years) of the thermal waters (pre-modern groundwater according to Clark et al., 1997)

Due to the large uncertainties affecting the chemical and physical processes (Plummer and Glynn, 2013), no carbon correction model was applied. Consequently, the water samples are considered as older than the uncorrected apparent ages. Therefore, the radiocarbon activities of the thermal waters ranges from 7.54 ± 0.8 to 8.45 ± 0.8 pmc corresponding to uncorrected ^{14}C ages varying from 19849 to 21050 BP (Table 1), implying that recharge may have occurred during late Pleistocene. On the other hand, the ^{14}C content obtained from a fresh water sample collected at well #6, far approximately 1 km north of thermal wells #1 and #2 (Fig. 2), provided an uncorrected age equal to 4268 BP, resulting very younger than the thermal ones.

In terms of sulphur isotopes, Fig. 14 shows the plot of $\delta\,^{34}S$ and $\delta\,^{18}O$ values, as collected in the sulphates from the thermal well waters (Table 4). These data are also displayed together with the ranges of the same isotopic ratios from groundwater samples, collected in different environments (Claypool et al., 1980; Utrilla et al., 1992; Clark and Fritz, 1997; Gunn et al., 2006). This plot indicates that the SCT sulphates are compatible with an interaction with Miocene evaporitic sediments that, in our case, can be related to the Messinian succession. Moreover, the isotope enrichment factor

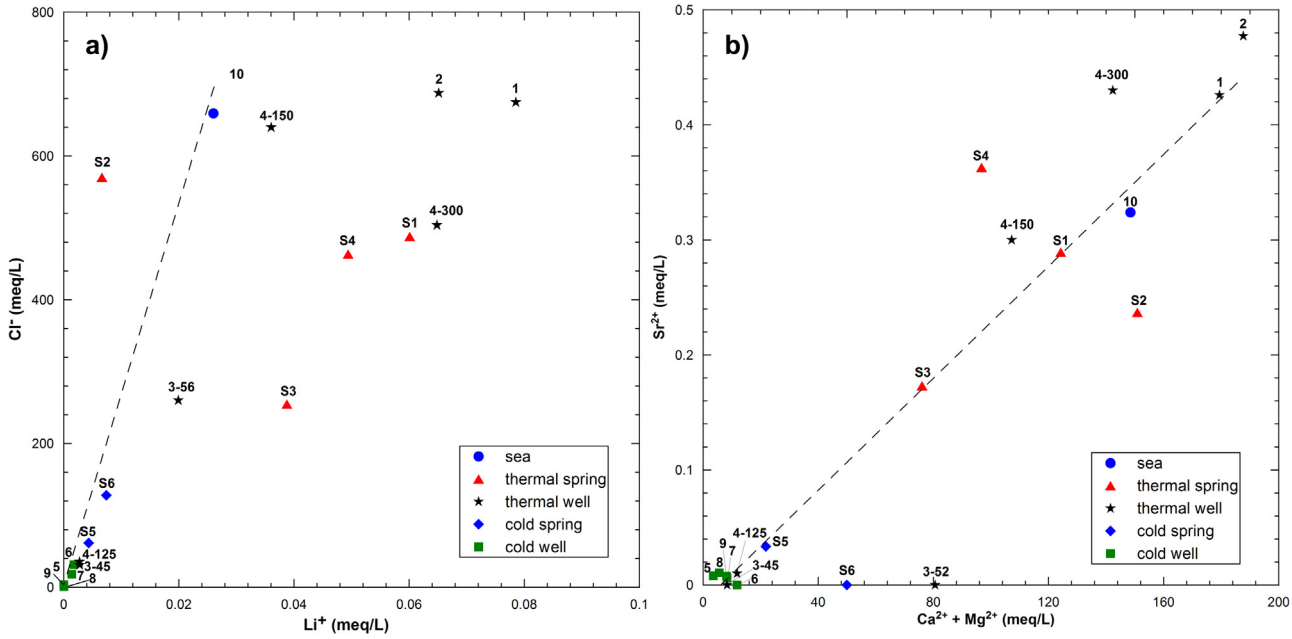

Fig. 12. Plot of Li^+ versus Cl^- (a) and of $Ca^{2+} + Mg^{2+}$ versus Sr^{2+} (b) concentrations in all sampled waters; data from Zuffianò et al. (2013) and new data.

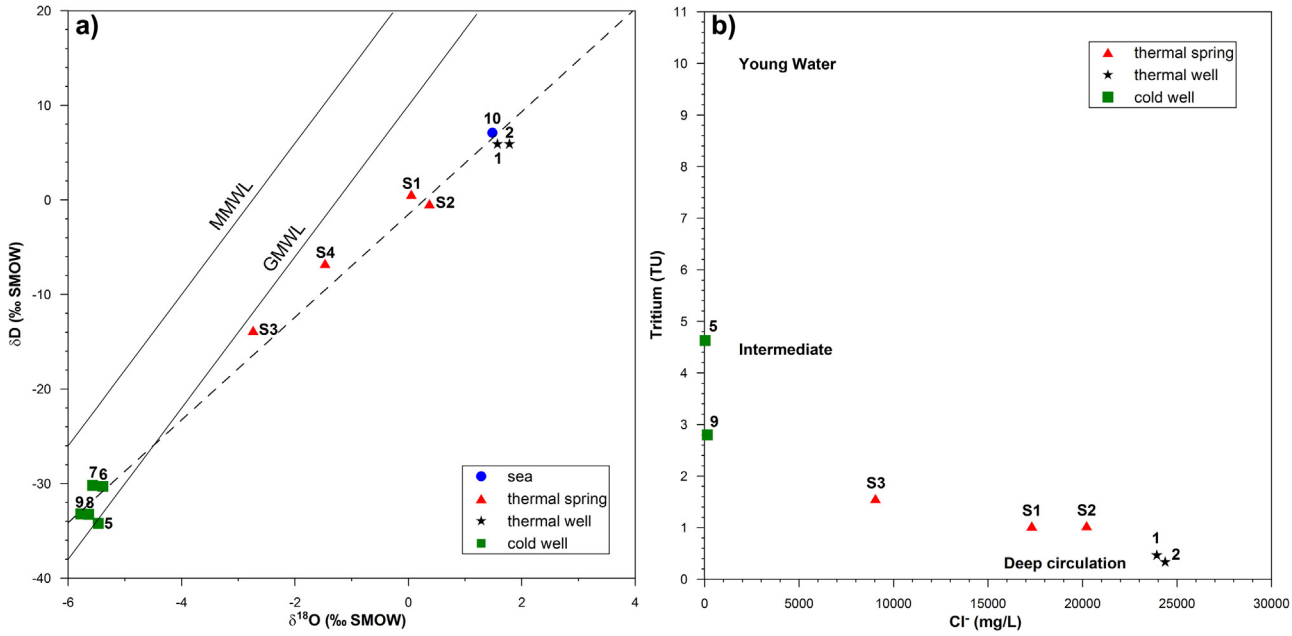

Fig. 13. (a) Binary δD–$\delta^{18}O$ diagram for water samples; (b) Tritium-Cl correlation plot for sampled waters; data from Zuffianò et al. (2013) and new data.

Table 4
Isotope values of groundwater sampled at the bottom of well 2 and 4.

Sample	$\delta^{18}O$	SO_4	$\delta^{34}S$	SO_4	$\delta^{34}S$	H_2S
	Result	Repeat	Result	Repeat	Result	Repeat
	VSMOW		VCDT			
2	12.79	12.32	21.67	21.71	−25.82	−26.03
4	11.72	11.81	20.66	20.38	−25.46	−25.36

ε, equal to 46.12‰, indicates a further bacterial sulphate reduction of dissolved sulphate (BSR; Wynn et al., 2010 and references herein).

Finally, the bulk of the thermal water samples plots in the field of partially equilibrated water, close to the immature waters field, within the Na-K-$Mg^{1/2}$ triangular diagram (Fig. 15), as proposed by Giggenbach (1988). This result implies a possible reservoir temperature encompassed between 160 and 180 °C. Only sample S3 indicates an immature water origin. Anyway, all the samples are far from the full equilibrium line, implying the geothermal water temperatures changed to a much greater extent during their re-equilibrium processes. Other reliable geothermometers indicate temperatures between 25 and 28 °C and 25–37 °C for the Mg–Li and Na–Li geothermometers (Kharaka and Mariner, 1989) respectively. Differently, a temperature of 44–49 °C is estimated by the quartz geothermometer (Fournier, 1977).

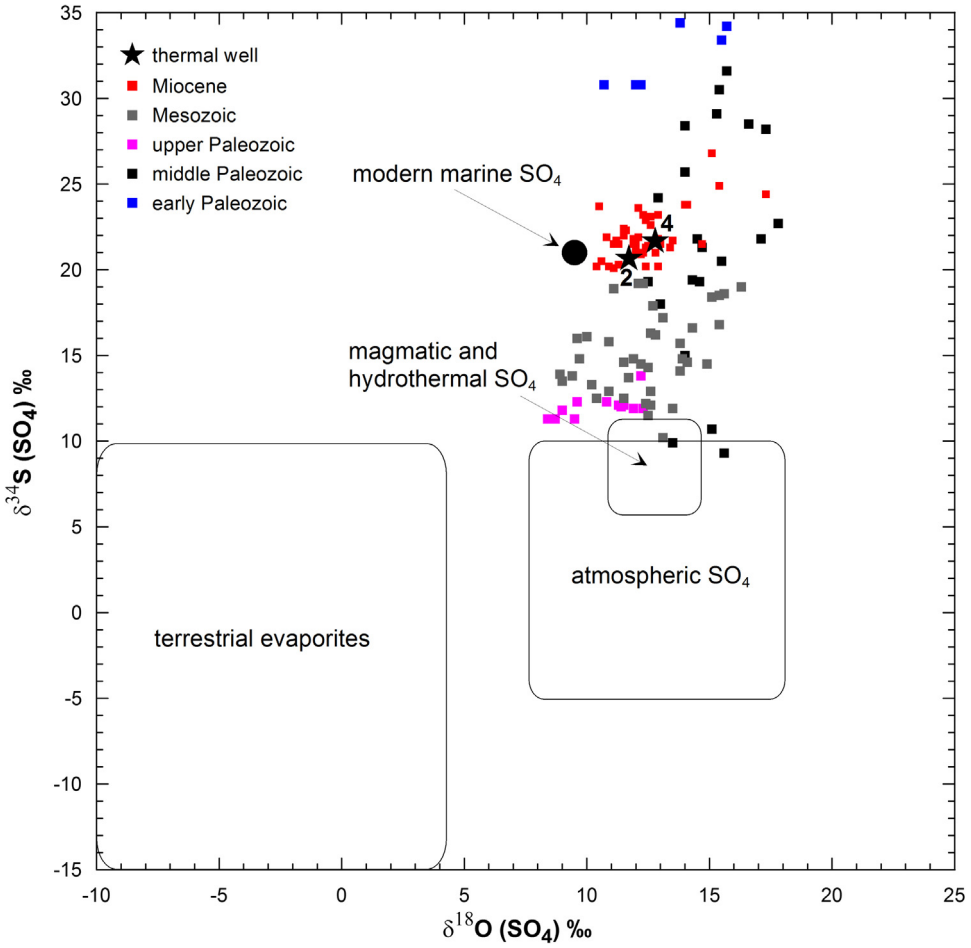

Fig. 14. Ranges of $\delta^{34}S$ and $\delta^{18}O$ values of sulphates of various origins dissolved in groundwater compared with thermal well water samples (literature data are after Claypool et al., 1980; Utrilla et al., 1992; Clark and Fritz, 1997; Palmer et al., 2004; Gunn et al., 2006).

5. Discussion

According to Calò and Tinelli (1995), the SCT thermal waters derive from upwelling seawaters through a system of closely spaced karsified tectonic fractures. Besides, the sulphate reduction of the seawater is to be related to reduction processes involving the organic matter bearing the calcareous rocks (Calò and Tinelli, 1995). Alternatively, organic substances and lignite content interlayered to Miocene outcrops can also interact with seawater giving rise to the same reduction processes (Zezza, 1980). Finally, a connate origin of the thermal waters was also envisaged (Maggiore and Pagliarulo, 2004).

Some remarks from the previous authors are partly confirmed by the present research (e.g. seawater origin and sulphate reduction) although implemented by new data and considerations. Firstly, all the obtained hydro-geochemical data, delimit the area where the geothermal anomaly occurs: this is 1 km along the coastline and 2 km wide inland (Fig. 7), corresponding to the most faulted portion of the SCT zone (Fig. 2), affected by Holocene, almost vertical, NW-SE transtensional faults. Apart from fractures, as seen in detailed geological survey, the area is characterized by extensional jogs, indicating localized higher permeability, possible improved by karst processes. In this view, the hydrothermal minerals in the veins (Figs. 4–5) testify to the structural influence on channelling fluids. A similar set of faults was recognized offshore of the Santa Cesarea Geothermal area (Del Ben et al., 2015): notably some of these structures are considered seismically active (INGV, 2006).

Water geochemistry indicates three main types of waters: (a) the pure fresh groundwater (sample 5 in Figs. 10–13a) deriving from meteoric infiltration and flow in the limestone aquifer without mixing with seawater intrusion; (b) brackish waters, from the partial mixing between fresh groundwater and saline groundwater due to seawater intrusion (e.g. samples 9, 8, 7, 6, 4–125, 4–151 in Figs. 10–13) produced by different amounts of seawater content (the highest in sample 4–151, Fig. 10); (c) thermal groundwater, occurring at depth (samples 1 and 2; Fig. 9). Thermal groundwater interacts with both fresh groundwater and saline groundwater of seawater intrusion, giving rise to variable chemical compositions, as it is the case from samples from Fetida and Gattulla caves (samples #S1 and #S3). For this reason, the geochemical features of the geothermal reservoir are defined by the chemical composition from wells #1 and #2 and #4 at depth (Fig. 10).

The chemical composition of the thermal waters can provide information on the fluid pathway. In fact, with respect to fresh groundwater and seawater, the higher Ca^{2+} and low Mg^{+} concentrations could derive from calcite dolomitization (Collins, 1975), as commonly it occurs in limestone. On the other hand, the increase of Ca^{2+} content could be related to the dissolution of gypsum or anhydrite, generally included in the Messinian evaporite where the concomitant bacterial SO_4^{2-} reduction can develop (Appelo and Postma, 1996).

Furthermore, the significant amount of Br and B contents could be the result of both organic matter decomposition (Martin et al., 1993; You et al., 1993) and water interaction with illite/smectite

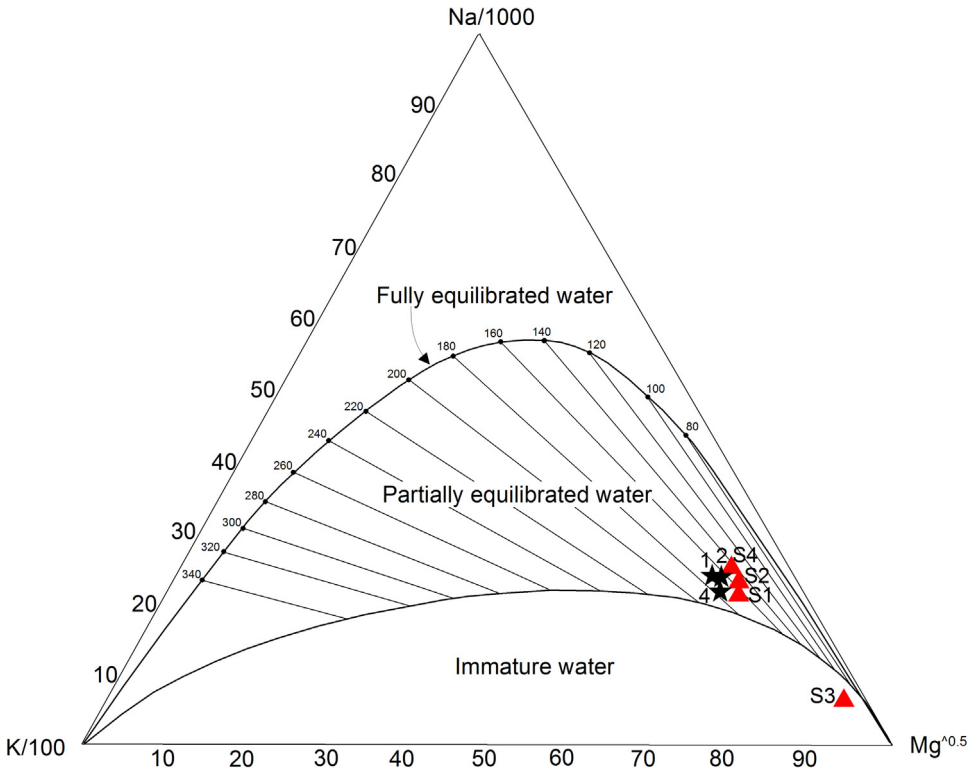

Fig. 15. Na/1000–K/100–$Mg^{1/2}$ ternary diagram (Giggenbach, 1988) applied to thermal waters.

clays (Kharaka and Hanor, 2003). Besides, boron tends to be concentrated in environments with a limited water circulation, such as the case of evaporite and brines (Uhlman, 1991). More other information on the fluid path is taken from the high Li^+ content of which amount indicates interaction with clay minerals (White, 1957; Paropkpari, 1990) or a long residence in reservoirs (Edmunds and Smedley, 2000). Even the high content of As estimated for the thermal waters respect to the other samples could be related to the water interaction with evaporitic minerals or rocks including limestone/dolomite (Dogan and Dogan, 2007).

The overall positive $\delta^{18}O$ and δD shift recorded by samples #1 and #2 should reflect the composition of an original seawater undergone evaporation effects (Boschetti et al., 2011; Clark and Fritz, 1997).

The geothermometers give a range of the temperature reservoir between 25 °C and 160 °C. Accepting the temperature upper limit of 80–110 °C given by the bacterial sulphate reduction (Machel, 2001; Wynn et al., 2010), this range narrows.

During the upwelling towards the springs' outflows, the deep thermal water, the lesser dense water in the SCT system due to the highest temperature, notwithstanding the highest salinity, breaks the barrier defined by the occurrence of both the intruded seawater (the more dense water) and the cold groundwater (denser than the thermal one but less dense than the intruded seawater). The higher piezometric levels recorded by the thermal wells (e.g. in well 4: 1 m a.s.l.) respect to the cold groundwater confirm in fact an upward flowing.

In this view, with the knowledge that the water density is a temperature and salinity function, and being the last parameter almost constant at depth (Fig. 7), thermal water temperature should be high enough to favour its upflowing. Based on the equation from McCutcheon et al. (1993), a temperature of 80 °C has been estimated as minimum necessary to promote the thermal water upflowing. Finally, based on the equation from Liu et al. (2015), the estimated circulation depth of 2200 m has been calculated considering, in the study area, the average temperature gradient of about 3 °C/100 m (Mongelli et al., 1983), a mean annual air temperature of about 18 °C and a depth of the constant-temperature zone of 30 m (Romanazzi et al., 2015).

6. Conclusion

Fig. 16 summarizes the hydrothermal circulation pathway for the SCT system as resulted from the integration of data, as previously described.

The recharge area is located offshore, at sea bottom, and, in this context, it is channelled through localized fault damages zones. Faults, affecting both the Miocene-Quaternary sediments and the underlying carbonate substratum, are supposed with a lateral to oblique component as indicated by focal mechanism on recent seismic events.

Moving downwards along the faulted zones, infiltrating seawater is heated (due to the geothermal gradient) and interacts with rocks of different origin (i.e. Messinian evaporates and Mesozoic-Oligocene limestone, mainly). The result is thus an enrichment, for instance, in calcium, sulphate, boron, sulphide and lithium elements, making the original seawater a thermal fluid, as indicated by oxygen isotope ratios, as well.

Thereafter, the geothermal waters, already heated by the geothermal gradient, are driven upwards by the buoyant forces generated by the density decrease. Along the almost vertical structural channels (e.g. extensional jogs) determined within the transtensional damage fault zones.

The circulation path here proposed here lasts a long time, roughly 20000 years as indicated by the geochronological analyses.

In conclusion,the SCT springs are evidence of a hydrothermal-convection system, where convection occurs within the fault damage zones (Fig. 16), passing through the Messinian deposits and

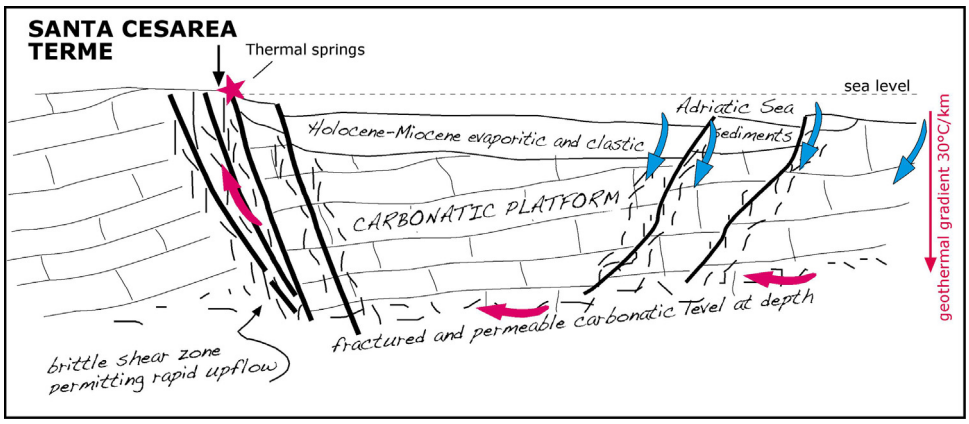

Fig. 16. Conceptual model (not to scale) of the relationships between brittle structures and fluid flow in the Santa Cesarea Terme area. The seawater is channelled (blue arrows) to depth through the damage zones of the faults affecting the sea-bottom down to the carbonate platform at depth, interacting mainly with Messinian evaporites and Mesozoic-Oligocene limestone. At a deeper structural level, a fractured and permeable level is supposed to host the marine water that has been infiltrated through the carbonate platform. Conversely, the fault system in Santa Cesarea determined a structural channel where the marine water, can rapidly upflows, maintaining a part of the temperature gained at depth. (For interpretation of the references to colour in this figure legend, the reader is referred to the web version of this article.)

the Mesozoic-Oligocene carbonate rocks, capped by the Holocene-Pliocene sediments. The original seawater therefore mostly resides at a depths of about 2–3 km, where it reaches a temperature of about 85 °C, from where it moves upwards, crossing the transition zone of the seawater intrusion.

Acknowledgments

The present activity has been performed in the frame of the VIGOR Project, aimed at assessing the geothermal potential and exploring geothermal resources of four regions in southern Italy. VIGOR is part of the activities of the Interregional Programme "Renewable Energies and Energy Savings FESR 2007–2013–Axes I Activity line 1.4 'Experimental Actions in Geothermal Energy'. The authors acknowledge the management of VIGOR Project, and in particular: Dr. Piezzo of MiSE-DGENRE (Directorate General for Nuclear Energy, Renewable Energy and Energy Efficiency of the Ministry for Economic Development); Dr. Brugnoli, Director of CNR-DTA (National Research Council of Italy, Department of Sciences of the Earth System and Environmental Technologies); the coordinator, Drs. Manzella from CNR-IGG. Thanks are also due to the whole staff of the Santa Cesarea Terme spa for the availability displayed during the research activities performed for the pilot site of the study.

We are deeply indebted with Ingrid Stober, an anonymous referee and with the Editor, David Bruhn: their comments and suggestions helped us to largely improve the original manuscript.

References

Appelo, C.A.J., Postma, D., 1996. Geochemistry, Groundwater and Pollution. A.A. Balkema Rotterdam, The Netherlands, 536 pp.

Ardizzone, F., Barnaba, F., Basso, A., Casarano, D., Dragone, D., Giornetti, L., Limoni, P., Liotta, D., Lollino, P., Pagliarulo, R., Palladino, G., Parise, M., Polemio, M., Romanazzi, A., Trizzino, R., Wasowski, J., Zuffianò, L.E., Rizzo, E., Minissale, A., Montanari, D., Montegrossi, G., Mussi, M., Cardellicchio, N., Aldighieri, B., De Franco, R., 2012. Rapporto Di Fattibilità Tecnica 1: Area Di Studio Santa Cesarea Terme. Progetto Vigor, All, 3, 37 pp.

Baietto, A., Cadoppi, P., Martinotti, G., Perello, P., Perrochet, P., Vuatez, F.D., 2008. Assessment of thermal circulation in strike-slip fault systems: the Terme di Valdieri case (Italian western Alps). The Internal Structure of Fault Zones: Implications for Mechanical and Fluid-flow Properties, 299. Geological Society London Special Publications, pp. 317–339.

Biginelli, P., 1899. Acque e fanghi delle grotte di S. Cesaria. Ann. di Farm Chim. 11–12, 490.

Boschetti, T., Toscani, L., Shouakar-Stash, O., Iacumin, P., Venturelli, G., Mucchino, C., Frape, S.K., 2011. Saltwaters of the northern apennine foredeep basin (Italy): origin and evolution. Aquat. Geochem. 17, 71–108.

Bosellini, A., Bosellini, F.R., Colalongo, M.L., Parente, M., Russo, A., Vescogni, A., 1999. Stratigraphic architecture of the Salento coast from Capo d'Otranto to Santa Maria di Leuca (Apulia, southern Italy). Riv. Italiana Paleontol. Stratigr. 105 (3), 397–416.

Bossio, A., Mazzei, R., Monteforti, B., Salvatorini, G., 2005. Stratigrafia del Neogene e Quaternario del Salento sud-orientale (con rilevamento geologico alla scala 1:25.000). Geol. Romana 38, 31–60.

Brogi, A., Cerboneschi, A., Lazzarotto, A., 2005. Geometry, stacking pattern and deformation timing of imbricate thrust-sheets within the Tuscan Nappe in the Travale area (Larderello geothermal area, Italy). Boll. Soc. Geol. Italiana 3, 73–87.

Calò, G., Tinelli, R., 1995. Systematic hydrogeological study of a hypothermal spring (S. cesarea terme apulia), Italy. J. Hydrol. 165, 185–205.

Clark, I.D., Fritz, P., 1997. Environmental Isotopes in Hydrogeology. Lewis Publishers, Boca Raton, FL.

Clark, W.B., Jenkins, W.J., Top, Z., 1997. Determination of tritium by mass spectrometric measurements. J. Appl. Radioact. Isotopes 27, 515–522.

Claypool, G.E., Holser, W.T., Kaplan, I.R., 1980. The age curves of sulfur and oxygen isotopes in marine sulfate and their mutual interpretation. Chem. Geol. 28, 199–260.

Collins, A.G., 1975. Geochemistry of Oilfield Waters. Developments in Petroleum Science 1. Elsevier Scientific Pubi. Comp., New York (496 pp).

Cotecchia, V., Studi e ricerche sulle acque sotterranee e sull'intrusione marina in Puglia (Penisola Salentina), Quaderni dell'Istituto di Ricerca sulle Acque, Consiglio Nazionale delle Ricerche, 1977 (345 pp).

Cotecchia, V., Grassi, D., Polemio, M., 2005. Carbonate aquifers in Apulia and seawater intrusion. Giornale di Geologia Applicata 1, 219–231.

Craig, H., Lupton, J.E., Horibe, Y., 1978. A mantle helium component in circum-pacific volcanic gases: hakone, the Marianas and Mt. Lassen. In: Alexander, E.G., Ozima, M. (Eds.), Terrestrial Rare Gases. Central Academic Publish., Tokio (Japan), pp. 3–16.

Craig, H., 1961. Isotopic variations in meteoric waters. Science 133, 1702–1703.

Del Ben, A., Mocnik, A., Volpi, V., Karvelisca, P., 2015. Old domains in the South Adria plate and their relationship with the West Hellenic. J. Geodyn. 89, 15–28.

Della Vedova, B., Bellani, S., Pellis, G., Squarci, P., 2001. Deep temperatures and surface heat flow distribution. In: Vai, G.B., Martini, L.P. (Eds.), Anatomy of an Orogen: the Apennines and Adjacent Mediterranean Basins. KluwerAcademic Publishers, pp. 65–76.

Di Bucci, D., Caputo, R., Mastronuzzi, G., Fracassi, U., Selleri, G., Sansò, P., 2011. Quantitative analysis of extensional joints in the southern adriatic foreland (Italy), and the active tectonics of the apulia region. J. Geodyn. 1–2, 141–155.

Dogan, M., Dogan, A.U., 2007. Arsenic mineralization, source, distribution, and abundance in the Kutahya region of the western Anatolia, Turkey. Environ. Geochem. Health 29, 119–129.

Edmunds, W.M., Smedley, P.L., 2000. Residence time indicators in groundwater: the East Midlands Triassic sandstone aquifer. Appl. Geochem. 15, 737–752.

Fanning, K.A., Byrne, R.H., Breland, J.A., Betzer, P.R., Moore, W.S., Elsinger, R.J., Pyle, T.E., 1981. Geothermal springs of the west Florida continental shelf: evidence for dolomitization and radionuclide enrichment. Earth Planet. Sci. Lett. 52, 345–354.

Favali, P., Mele, G., Mattietti, G., 1990. Contribution to the study of the Apulian microplate geodynamics. Memorie Soc. Geol. Italiana 44, 71–80.

Finetti, I.R., 2005. In: Finetti, I.R. (Ed.), CROP Project: Deep Seismic Exploration of the Central Mediterranean and Italy. Atlases in Geoscience 1, Elsevier, p. 794.

Fournier, R.O., 1977. Chemical geothermometers and mixing models for geothermal systems. Geothermics 5, 41–50.

Gatt, J.R., Carmi, I., 1970. Evolution of the isotopic composition of atmospheric waters in the Mediterranean Sea area. J. Geophys. Res. 75, 3032–3048.
Giggenbach, W.F., 1988. Geothermal solute equilibria: derivation of Na-K-Mg-Ca geoindicators. Geochim. Cosmochim. Acta 52, 2749–2765.
Goldstein, B.A., Hiriart, J.W., Tester, R., Bertani, C.J., Gutiérrez-Negrín, E., Huenges, A., Ragnarsson, M.A., Muraoka, H., Zui, V.I., 2011. Great expectations for geothermal energy to 2100. In: Proceedings of the Thirty-Sixth Workshop of Geothermal Reservoir Engineering, Stanford University, Stanford, CA, 31 January ?2 February 2011, SGP-TR-191, pp. 5–12.
Grasby, S.E., Hutcheon, I., 2001. Controls on the distribution of thermal springs in the southern Canadian Cordillera. Can. J. Earth Sci. 38 (3), 427–440.
Gunn, J., Bottrell, S.H., Lowe, D.J., Worthington, S.R.H., 2006. Deep groundwater flow and geochemical processes in limestone aquifers: evidence from thermal waters in Derbyshire, England, UK. Hydrogeol. J. 14, 868–881.
INGV, 2006. Mappa di pericolosità sismica di riferimento per il territorio nazionale. In: OPCM 28 Aprile 2006, n. 3519, Criteri Generali Per l'individuazione Delle Zone Sismiche E Per La Formazione E l'aggiornamento Degli Elenchi Delle Medesime Zone, All. 1b, G.U. n. 108 del 11 maggio 2006, Roma.
Kharaka, Y.K., Hanor, J.S., 2003. Deep fluids in the continents: I. sedimentary basins. Treat. Geochem. 5 (9), 1–48.
Kharaka, Y.K., Mariner, R.H., 1989. Chemical geothermometers and their application to formation waters from sedimentary basins. In: Naser, N.D., McCulloh, T.H. (Eds.), Thermal History of Sedimentary Basins; Methods and Case Histories. Springer New York, pp. 99–117.
Liu, Y., Zhoua, X., Deng, Z., Fanga, B., Tsutomue, Y., Zhaoa, J., Wanga, X., 2015. Hydrochemical characteristics and genesis analysis of the Jifeihot spring inYunnan, southwestern China. Geothermics 53, 38–45.
Machel, H.G., 2001. Bacterial and thermochemical sulfate reduction in diagenetic settings – old and new insights. Sediment. Geol. 140, 143–175.
Maggiore, M., Pagliarulo, P., 2004. Circolazione idrica ed equilibri idrogeologici negli acquiferi della Puglia. Geologi Territorio 1, 13–35.
Martin, J.B., Gieskes, J.M., Torres, M., Kastner, M., 1993. Bromine and iodine in Peru margin sediments and pore fluids: implications for fluid origins. Geochim. Cosmochim. Acta 57, 4377–4389.
McCutcheon, S.C., Martin, J.L., Barnwell Jr., T.O., 1993. Water quality. In: Maidment, D.R. (Ed.), Handbook of Hydrology. McGraw-Hill, New York, NY.
Milani, M., 1815. Cenni geologici sulla Provincia di Terra d'Otranto. Napoli.
Minissale, A., Vaselli, O., 2011. Karst springs as natural pluviometers: constraints on the isotopic composition of rainfall in the Apennines of central Italy. Appl. Geochem. 26, 838–852.
Minissale, A., 2004. Origin, transport and discharge of CO2 in central Italy. Earth Sci. Reviews 66, 89–141.
Mocnik, A., 2008. Metodologie geofisiche integrate per la correlazione tra strutture superficiali e profonde nel Canale di Otranto. Degree Thesis, University of Trieste, 1–141.
Mongelli, F., Ciaranfi, N., Tramacere, A., Zito, G., Perusini, P., Squaraci, P., Taffi, L., 1983. Contributo Alla Mappa Del Flusso Geotermico in Italia: Misure Dalle Marche Alla Puglia 2° Convegno Annuale Del Gruppo Nazionale Di Geofisica Della Terre Solida, Roma.
Mostardini, F., Merlini, S., 1986. Appennino centro meridionale: sezioni geologiche e proposta di modello strutturale. Memorie Soc. Geol. Italiana 35, 177–202.
Muffler, L.P.J., Cataldi, R., 1978. Methods for regional assessment of geothermal resources. Geothermics 7, 53–89.
Nicolich, R., 2001. Deep seismic transects. In: Vai, G.B., Martini, I.P. (Eds.), Anatomy of an Orogen, the Apennines and Adjacent Mediterranean Basins. Dor-drecht, Kluwer Academic Publishers, pp. 47–52.
Palmer, M.R., Helvaci, C., Fallick, A.E., 2004. Sulfur, sulfate oxygen and strontium isotope composition of Cenozoic Turkish evaporites. Chem. Geol. 209, 341–356.
Paropkpari, A.L., 1990. Geochemistry of sediments from the Mangalore-Cochin shelf and upper slope off south-west India geological and environmental factors controlling dispersal of elements. Chem. Geol. 81, 99–119.
Patacca, E., Scandone, P., 2007. Geology of the southern apennines. Italian J. Geosci., Special Issue No. 7, 75–119.
Pepe, M., Parise, M., 2013. Structural control on development of karst landscape in the Salento Peninsula (Apulia, SE Italy). Acta Carsol. 43 (1), 101–114.
Plummer, L.N., Glynn, P.D., 2013. Radiocarbon dating in groundwater systems. In Isotope methods for dating old groundwater. In: Suckow, A., Aggarwal, P., Araguas-Araguas, L. (eds.), 33–90.
Polemio, M., Dragone, V., Limoni, P.P., 2009. Monitoring and methods to analyse the groundwater quality degradation risk in coastal karstic aquifers (Apulia, Southern Italy): Environmental Earth Sciences (formerly Environmental Geology) 58 (2), 299–312.
Pomar, L., Mateu-Vicens, G., Morsilli, M., Brandano, M., 2014. Carbonate rampevolution during the late oligocene (Chattian) salento peninsula, southern Italy. palaeogeography, palaeoclimatology. Palaeoecology 404, 109–132.
Purnomo, B.J., Pichler, T., 2014. Geothermal systems on the island of Java, Indonesia. J. Volcanol. Geotherm. Res. 285, 47–59.
Ricchetti, G., Ciaranfi, N., Luperto Sinni, E., Mongelli, F., Pieri, P., 1988. Geodinamica ed evoluzione sedimentaria e tettonica dell'Avampaese Apulo. Memorie della Società Geologica Italiana 41, 57–82.
Rolker, J., Schill, E., Stober, I., Schneider, J., Neumann, T., Kohl, T., 2015. Hydrochemical characterisation of a major central European heat flux anomaly: the Bürchau geothermal spring system Southern Black Forest, Germany. Geother. Energy 3 (5), 1–18.
Romanazzi, A., Polemio, M., Gentile, F., 2015. Modelling and management of a Mediterranean karstic coastal aquifer under the effects of seawater intrusion and climate change. Environ. Earth Sci. 74, 115–128.
Roveri, M., Flecker, R., Krijgsman, W., Lofi, J., Lugli, S., Manzi, V., Sierro, F.J., Bertini, A., Camerlenghi, A., De Lange, G., Govers, R., Hilgen Frits, J., Hübscher, C., Meijer P.Th. Stoica, M., 2014. The Messinian Salinity Crisis: past and future of a great challenge for marine sciences. Mar. Geol. 352, 25–58.
Sivan, O., Yechieli, Y., Herut, B., Lazar, B., 2005. Geochemical evolution and timescale of seawater intrusion into the coastal aquifer of Israel. Geochim. Cosmochim. Acta 69 (3), 579–592.
Uhlman, K., 1991. The geochemistry of boron in a landfill monitoring program. Ground Water Monit. Rev. 11, 139–143.
Utrilla, R., Pierre, C., Orti, F., Pueyo, J.J., 1992. Oxygen and sulphur isotope composition as indicators of the origin of Mesozoic and Cenozoic evaporites from Spain. Chem. Geol. 102, 229–244.
ViDEPI Project (Visibility of Petroleum Exploration Data in Italy), 2009. Visibility of Petroleum Exploration Data in Italy. http://unmig. sviluppoeconomico.gov.it/videpi/en/default.htm.
Visintin, B., 1944. Studio sull'acqua della Grotta Gattulla delle Terme demaniali di S. Cesarea. Rendiconti Istituto Superiore Sanità 7 (2).
White, D.E., 1957. Magmatic, connate, and metamorphic waters. Bull. Geol. Soc. America 68, 1659–1682.
Wynn, J.G., Sumrall, J.B., Onac, B.P., 2010. Sulfur isotopic composition and the source of dissolved sulfur species in thermo-mineral springs of the Cerna valley, Romania. Chem. Geol. 271, 31–43.
You, C.F., Gieskes, J.M., Chen, R.F., Spivack, A.J., Gamo, T., 1993. Iodide, bromide, manganese, boron, and dissolved organic carbon in interstitial of organic carbon-rich marine sediments: observations in Nankai accretionary prism. Proc. ODP Init. Reports 131, 165–174.
Zezza, F., 1980. Le sorgenti ipotermali solfuree di Santa Cesarea Terme. Salentum, Azienda di cura, soggiorno e turismo, Santa Cesarea Terme, anno III, n. 1–2, (37 pp.).
Zuffianò, L.E., Palladino, G., Santaloia, F., Polemio, M., Liotta, D., Limoni, P.P., Parise, M., Pepe, M., Casarano, D., Rizzo, E., Minissale, A., De, Franco, R., Geothermal resource in a foreland environment: the Santa Cesarea Terme thermal springs (Southern Italy). In: European Geothermal Congress 2013, Pisa, Italia, 3–7/06/2013, p. 101–104, ISBN: 978-2-8052-0226-1.